PHYSICAL REVIEW A VOLUME 52, NUMBER 1 JULY 1995

Pattern formation in a liquid-crystal light valve with feedback, including polarization, saturation, and internal threshold effects

R. Neubecker and G.-L. Oppo
Department of Physics and Applied Physics, University of Strathclyde, 107 Rottenrow, Glasgow G4 0NG, Scotland

B. Thuering and T. Tschudi
Institut fuer Angewandte Physik, Technische Hochschule Darmstadt, Hochschulstrasse 6, 62498 Darmstadt, Germany

(Received 28 November 1994)

The use of liquid-crystal light valves (LCLV's) as nonlinear elements in diffractive optical systems with feedback leads to the formation of a variety of optical patterns. The spectrum of possible spatial instabilities is shown to be even richer when the LCLV's capability for polarization modulation is utilized and internal threshold and saturation effects are considered. We derive a model for the feedback system based on a realistic description of the LCLV's internal function and coupling to a polarizer. Thresholds of pattern formation are compared to the common Kerr-type approximation and show transitions involving rolls, squares, hexagons, and tiled patterns. Numerical and experimental results confirm our theoretical predictions and unveil how patterns and their typical length scales can be easily controlled by changes of the parameters.

PACS number(s): 42.65.Pc, 42.50.Ne, 42.82.Fv, 42.50.Gy

I. INTRODUCTION

Spontaneous pattern formation in the transverse domain of nonlinear optical devices is attracting a growing interest not only for its relevance to fundamental physics but also for possible applications to optical information technology [1–5]. Many theoretical, computational, and experimental studies have demonstrated the universality of the coupling of diffraction and optical nonlinearities to generate patterns with a considerable degree of spatiotemporal complexity. Lasers, optical parametric oscillators, Kerr and saturable nonlinearities, liquid-crystal light valves (LCLV's), photorefractive materials, and many others have been utilized to display the universality of optical pattern formation [1–6].

In spite of this remarkable success, quantitative agreement between models and experiments is still lacking, making the exploitation of optical patterns for applications a nontrivial task. One of the main difficulties arises in the design of an optical system flexible (complex) enough to display a large variety of spatiotemporal behaviors, yet simple enough to be accurately described by models of few partial differential equations. It is the aim of this paper to show that the use of LCLV's in simple feedback configurations, with the inclusion of polarization control, displays the richest versatility of pattern generation to date and can be accurately modeled by equations easy to integrate numerically. We also present the experimental realization of large aspect ratio patterns and the control of their spatial scales.

LCLV's have been used to study the onset of optical patterns for some time [7–17], often including geometrical transformations such as rotations in the feedback. Recently, however, interest has shifted to simplified schemes with higher symmetry, which use these devices to approximately realize the arrangement of a single feedback Kerr slice setup [12,13,15–17], following the suggestions of Firth and D'Alessandro [18–22].

LCLV's are optically addressable spatial modulators and were designed originally for display applications [23–26]. Such applications always make use of the LCLV's ability of polarization modulation, which is transformed into an amplitude-intensity modulation by use of a polarizer. More recent experiments, however, have been limited to sole phase modulation. LCLV's have great experimental advantages with respect to other passive nonlinearities: these include high modulation sensitivity (allowing for the use of low power lasers), large space-bandwidth product (i.e., large transverse aspect ratio), and slow time scales (allowing for simple recording of the pattern dynamics). A LCLV can be regarded as an optical nonlinearity with spatially separated interaction light-matter and matter-light.

Theoretical and computational studies of pattern formation in single feedback systems have often been based on Kerr nonlinearities. LCLV's in experimental setups have been shown to display such a type of nonlinearity [10]. While we recognize that this is a reasonable approximation to describe qualitative features of the experimental results, LCLV's present a far wider flexibility in terms of pattern formation whenever a more careful treatment of the underlying physics is taken into consideration. Moreover, a quantitative comparison between experimental and theoretical results becomes available. In the following we generalize a previous theoretical approach to LCLV's with feedback in order to include polarization modulations as well as saturation and internal threshold effects. We show that these effects lead to unexpected and intriguing forms of pattern generation. More important, the main deviations of our theoretical approach from the Kerr approximation are shown to be in consistent and in quantitative agreement with exper-

1050-2947/95/52(1)/791(18)/$06.00

iments. A LCLV system including polarization modulation, but not saturation and internal threshold effects, has been discussed briefly in [14].

The generalization of the LCLV model means that part of the simplicity of the Kerr approximation is lost. For example, the number of independent parameters increases. This corresponds, however, to a larger amount of experimental control of the process of pattern formation, a considerable advantage with respect to previous studies. By selecting physical values of the parameters, we present generic sequences of pattern generation, modification, and competition.

The paper is organized as follows. In the next section, the diffractive feedback to the LCLV is described mathematically and the effects of polarization modulation included in the model equations. In Sec. III we provide a short review of the operation of the LCLV and details about the inclusion of the internal processes of the LCLV in the model. The homogeneous steady state solutions are described in Sec. IV. A linear stability analysis to determine the threshold of pattern formation is provided in Sec. V. The results of extensive numerical simulations are presented in Sec. VI and are later compared with experimental results in Sec. VII. A short discussion and conclusions are presented in Sec. VIII.

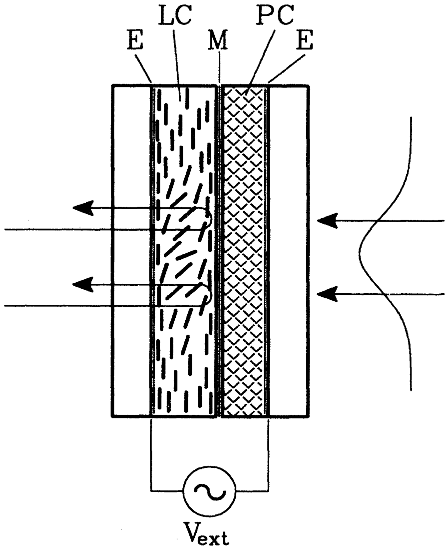

FIG. 1. Liquid-crystal light valve: LC: liquid-crystal layer, M: mirror, PC: photoconductor layer, E: transparent electrodes. The reorientation of the liquid-crystal molecules according to an intensity distribution incident on the write side from the right is indicated.

II. DESCRIPTION OF THE FEEDBACK

The type of reflective LCLV considered here consists of a write side sensitive to the light intensity [photoconductor layer (PC)], and a birefringent, phase modulating, read-out side [liquid-crystal layer (LC)] (see Fig. 1). The spatial intensity distribution of the write beam is transformed into a corresponding phase and, possibly, polarization modulation of the read-out light beam. The basic idea behind the feedback operation is that a homogeneous pump wave reads out the changes of refractive index in the LCLV and then, after passing through the polarizer and propagating freely over a finite distance L, feeds back the information on the write side of the LCLV. The schematic feedback setup is shown in Fig. 2 while the corresponding unfolded and simplified scheme is shown in Fig. 3. Lenses are used to image the LCLV read-out plane. If the image plane $P1$ is located in front of the write plane (see Fig. 2), the feedback wave propagates freely over a length L before reaching the write side. The resulting diffraction induces spatial instabilities and pattern formation, as will be closely investigated in the following sections. Diffraction can be prevented by imaging the read-out beam onto the write side exactly ($L = 0$). By locating the image plane behind the LCLV it is also possible to exploit an intrinsic symmetry of the system and simulate a self-focusing nonlinearity [27,28] (see the end of Sec. III for more details).

Typical time constants τ of the LCLV are in the range of some ten milliseconds while it takes the light wave only some nanoseconds to travel through the feedback loop. Because of this large separation of time scales, the feedback is assumed to be instantaneous. On the time scale of wave propagation, the LCLV is considered stationary and the dynamics of the light field neglected. After passing through the LCLV, the input electric field $E_{\rm in}$ is phase modulated and its polarization changed. Then, a polarizer is used to transfer the polarization modulation into an amplitude modulation. These processes can be conveniently described via the Jones calculus [29]. The 2×2 matrices $\mathcal{M}$ and $\mathcal{P}$ describe the action of the LC layer and the polarizer, respectively,

$$\vec{E}_m = \mathcal{P}\mathcal{M}\vec{E}_{\rm in} = (\vec{B}e^{-i\phi} + \vec{C})E_{\rm in} \ , \qquad (1)$$

where

$$\mathcal{P} = \begin{pmatrix} \cos^2\psi_2 & \sin\psi_2\cos\psi_2 \\ \sin\psi_2\cos\psi_2 & \sin^2\psi_2 \end{pmatrix}, \quad \mathcal{M} = \begin{pmatrix} e^{-i\phi} & 0 \\ 0 & 1 \end{pmatrix},$$
$$\vec{B} = \cos\Psi_1\cos\Psi_2 \begin{pmatrix} \cos\Psi_2 \\ \sin\Psi_2 \end{pmatrix}, \qquad (2)$$
$$\vec{C} = \sin\Psi_1\sin\Psi_2 \begin{pmatrix} \cos\Psi_2 \\ \sin\Psi_2 \end{pmatrix},$$

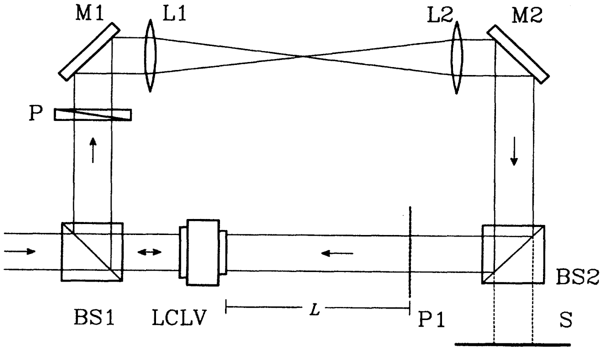

FIG. 2. Scheme of feedback setup: the beam splitters BS1, BS2, and the mirrors guide the modulated wave to the LCLV's write side, thereby passing the polarizer P. The lenses $L1$, $L2$ image the read-out side onto the plane $P1$, the feedback wave can be observed at the screen S.

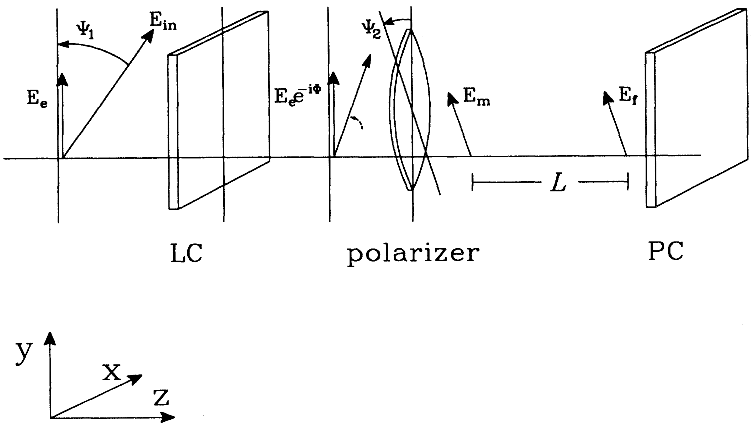

FIG. 3. Unfolded setup. The pump beam $E_{\rm in}$ coming from the left passes through the liquid-crystal layer (LC), where the extraordinary polarization experiences the phase shift ϕ. The beam then passes the polarizer and the phase and intensity modulated wave E_m propagates over a length L before reaching the photoconductor (PC).

and where ϕ is the nonlinear phase shift introduced by the LCLV (see the next section for details about its evolution equation), $\vec{E}_m$ is the amplitude of the modulated wave after passing through the polarizer (see Fig. 3), Ψ_1 is the angle of the input polarization, and Ψ_2 is the angle of the polarizer axis, both with respect to the optical axis of the LC layer.

In order to get an overview of the system's basic properties, we have selected some representative cases: (a) sole phase modulation corresponding to $\Psi_1 = \Psi_2 = 0$, (b) maximum polarization modulation corresponding to $\Psi_1 = -\Psi_2 = 45°$, and (c) an intermediate case of $\Psi_1 = -\Psi_2 = 22.5°$.

After the polarizer, the vector character of the wave is no longer relevant and free space propagation can be described via the stationary, scalar, paraxial wave equation:

$$\nabla_\perp^2 E - 2ik\frac{\partial}{\partial z}E = 0, \tag{3}$$

where k is the wave number of the light field. From this equation we can define a diffraction operator $\mathcal{D}$ by using $E(z = L) = \mathcal{D}\{E(z = 0)\}$ for the propagation over a distance L. A formal solution of (3) is

$$E_f = \mathcal{D}\{E_m\} = e^{-i(L/2k)\nabla_\perp^2}\{E_m\}, \tag{4}$$

where E_f denotes the amplitude of the feedback wave resulting from the diffracted and modulated wave E_m (see Fig. 3).

To close the feedback loop, we make the intensity of the feedback wave equal to the write intensity of the LCLV:

$$I_w = I_f \equiv |E_f|^2 = |e^{-i\hat{\nabla}_\perp^2}\{(Be^{-i\phi} + C)E_{\rm in}\}|^2, \tag{5}$$

where now the transverse space coordinates have been rescaled via

$$\hat{x} = \sqrt{\frac{2k}{L}}\,x, \quad \hat{y} = \sqrt{\frac{2k}{L}}\,y, \tag{6}$$

so that

$$\hat{\nabla}_\perp^2 = \frac{L}{2k}\nabla_\perp^2, \quad \hat{l} = \sqrt{\frac{2k}{L}}\,l. \tag{7}$$

The feedback intensity I_f is also the intensity distribution observed at the output of the setup displayed in Fig. 2.

III. PRINCIPLES OF OPERATION OF THE LIQUID-CRYSTAL LIGHT VALVE

A schematic diagram of a reflective LCLV is presented in Fig. 1. The liquid crystal and photoconductor layers are separated by a dielectric mirror, so that the read-out beam, being reflected at the internal mirror, passes twice through the liquid-crystal layer. Across both layers an external low-frequency ac voltage $V_{\rm ext}$ is applied via two transparent electrodes. The resulting electrical field transfers the information about the intensity distribution of the write beam from the PC layer to the LC layer. By changing the number of charge carriers, the impedance of the PC layer is locally reduced according to the local intensity of the write beam, leading to an increase of the electrical field across the LC layer. For simplicity we consider a linear change of the local voltage $V_{\rm LC}$ across the LC layer with the write intensity I_w, i.e.,

$$V_{\rm LC} = (\kappa_d + \kappa_i I_w)V_{\rm ext}, \tag{8}$$

where κ_d is the adimensional proportionality between $V_{\rm LC}$ and the external voltage in the absence of light while κ_i rules the linear dependence on I_w. Both κ_d and κ_i depend on the device and on the frequency of the external ac voltage $V_{\rm ext}$.

Because of the reorientation of the liquid-crystal molecules, the LC layer acts like an optical retarder plate, where the refractive index of the slow axis (the extraordinary beam) depends on the voltage $V_{\rm LC}$ and thus on the intensity distribution on the write side. The read-out wave correspondingly experiences a phase and polarization modulation that depends on the angle Ψ_1 between the optical axis of the LC layer and the polarization of the input beam. In general, a linearly polarized input beam becomes elliptically polarized after passing through the LC. The action of the LC layer is not instantaneous because of viscous damping of the molecule rotation and of internal RC time constants. There is also a spatial coupling, mainly resulting from lateral diffusion of the charge carriers in the PC layer [26,30]. It is possible to consider the LCLV as a slow, diffusive, and dispersive optical nonlinearity with spatially separated interaction light → matter (writing process) and matter → light (read-out process).

Our model of the LC layer considers a parallel aligned nematic liquid crystal where all molecules look like long rods, their long axes being initially oriented parallel to each other and to the glass substrate (see Fig. 1). Under the action of an electrical field perpendicular to their long axis, the molecules experience a torque trying to reorient them parallel to the field and therefore perpendicular to the surface. However, strong intramolecular (elastic) forces which are typical of the liquid-crystalline phase are also present. Their effect is to couple the orientation between adjacent molecules. Since the molecules at the surface have a fixed orientation (generally referred to as strong anchoring), the elastic forces counteract the action of the external field. In particular, this generates a threshold behavior ("Fréedericksz transition") [23,24,31,32] which corresponds to no reorientation below a certain critical value of the local voltage V_{LC}. Above such threshold, a continuous change in the reorientation of the molecules is found when increasing the field. The saturated state is reached when almost all molecules are oriented parallel to the external field. Since the effective refractive index n decreases with the write intensity, we are in the presence of a defocusing type of nonlinearity. The reorientation of the molecules can be described in terms of a mean angle which represents the rotation of the molecules' long axis averaged over the layer thickness [33]:

$$\bar{\theta} = \begin{cases} 0 & \text{for } V_{\mathrm{LC}} < V_{\mathrm{th}} \\ \dfrac{\pi}{2} - 2\arctan\left(-\dfrac{V_{\mathrm{LC}} - V_{\mathrm{th}}}{V_0}\right) & \text{for } V_{\mathrm{LC}} \geq V_{\mathrm{th}} \ , \end{cases} \tag{9}$$

where V_{th} is the threshold voltage. Both V_{th} and V_0 depend on the specific parameters and on the thickness d of the LC layer.

Optically, the LC layer appears as a thin, uniaxially birefringent layer. The effective refractive index n for the extraordinary wave is related to the reorientation angle by [34]

$$\frac{1}{n^2} = \frac{\cos^2\bar{\theta}}{n_e^2} + \frac{\sin^2\bar{\theta}}{n_o^2}, \tag{10}$$

where n_e and n_o are the extraordinary and ordinary refractive indices, respectively. For small differences $\Delta n = n_e - n_o$ (typically of the order of 0.2), we can approximate (10):

$$n \simeq n_o + \Delta n \cos^2\bar{\theta}, \tag{11}$$

so that the total phase difference ϕ between extraordinary and ordinary waves reads

$$\phi = \phi_{\max} \begin{cases} 1 & \text{for } V_{\mathrm{LC}} < V_{\mathrm{th}} \\ \cos^2\left[\dfrac{\pi}{2} - 2\arctan\left(-\dfrac{V_{\mathrm{LC}} - V_{\mathrm{th}}}{V_0}\right)\right] = 1 - \tanh^2\left(\dfrac{V_{\mathrm{LC}} - V_{\mathrm{th}}}{V_0}\right) & \text{for } V_{\mathrm{LC}} \geq V_{\mathrm{th}} \ , \end{cases} \tag{12}$$

where $\phi_{\max} \equiv 2kd\Delta n$ with k being the light wave number. This function is displayed in Fig. 4. Note that in this and all following figures all variables and parameters are dimensionless unless specified otherwise. Because of the negative slope of the saturation function, a positive $\phi_{\max}$ belongs to a self-defocusing nonlinearity. Making use of (8), we now replace the internal voltages by

$$\begin{aligned} \frac{V_{\mathrm{LC}} - V_{\mathrm{th}}}{V_0} &\simeq \left[\frac{V_{\mathrm{ext}}}{V_0}\kappa_i\right] I_w + \left[\frac{\kappa_d V_{\mathrm{ext}} - V_{\mathrm{th}}}{V_0}\right] \\ &\equiv \mu_s I_w + J_b \ , \end{aligned} \tag{13}$$

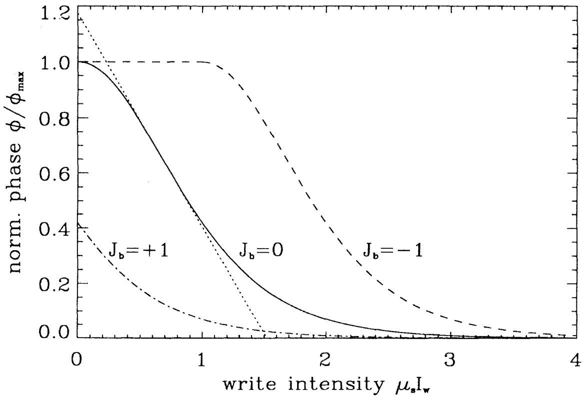

FIG. 4. Saturation function of phase depending on write intensity for different values of the bias intensity J_b. The linear (Kerr) approximation at the turning point is also shown.

where we have defined

$$\mu_s \equiv \frac{\kappa_i V_{\mathrm{ext}}}{V_0}, \quad J_b \equiv \frac{\kappa_d V_{\mathrm{ext}} - V_{\mathrm{th}}}{V_0} \ . \tag{14}$$

It should be pointed out here that even if J_b looks like an intensity ("bias intensity"), it does not correspond to a physical intensity of a light wave, but it is proportional to the external voltage. While $\phi_{\max}$ is fixed by the device, J_b is an easily accessible control parameter in an experiment. In the following, $\phi_{\max}$ is kept constant to the value 5π corresponding, for example, to a LC layer thickness of $d = 10\,\mu$m and a birefringence of $\Delta n = 0.08$ for a light wavelength of 633 nm.

By heuristically including the limited spatial and temporal resolution of the LCLV, we obtain the following expression [7,8,26]:

$$\tau\frac{\partial}{\partial t}\phi - l^2\nabla_\perp^2\phi + \phi$$

$$= \phi_{\max}\begin{cases} 1 & \text{for } (\mu_s I_w + J_b) < 0 \\ 1-\tanh^2(\mu_s I_w + J_b) & \text{for } (\mu_s I_w + J_b) \geq 0 \end{cases} \tag{15}$$

where $\nabla_\perp^2 = \frac{\partial^2}{\partial x^2} + \frac{\partial^2}{\partial y^2}$ is the transverse Laplacian. The effective time constant τ and the effective diffusion length l depend on the actual device and on the operating conditions [26,30].

In the past, LCLV's have been described via a linear dependence of the induced phase on the write intensity

$$\tau\frac{\partial}{\partial t}\phi - l^2\nabla_\perp^2\phi + \phi = \mu_k I_w + \phi_0 \ , \tag{16}$$

where ϕ_0 is the initial phase for vanishing I_w and μ_k is the modulation sensitivity. Under this approximation, LCLV's are equivalent to a slow, diffusive, Kerr-type nonlinearity, since Eq. (16) is similar to the models used to describe various Kerr media [35–37]. Figure 4, however, clearly shows that a linear approximation of the saturation function can have a limited justification, only. In fact, nearly the full range of $0 \leq \phi \leq \phi_{\max}$ is often accessible experimentally. In the following, we will discuss main differences between the Kerr approximation (16) and the model (15) based on the more appropriate description. One possibility to linearly approximate the saturation function (15) is to expand around the turning point as shown in Fig. 4, obtaining the following relations between the coefficients:

$$\mu_k \simeq -\frac{4\phi_{\max}}{3\sqrt{3}}\mu_s, \tag{17}$$

$$\phi_0 \simeq \phi_{\max}\left[\frac{2}{3} + \frac{4}{3\sqrt{3}}\ln\left(\frac{1+\sqrt{3}}{\sqrt{2}}\right) - \frac{4}{3\sqrt{3}}J_b\right] .$$

Finally, by inserting (5) into (15), or into (16) for the approximated Kerr case, the description of the LCLV feedback system is reduced to a single equation for the free variable $\phi(x,y,t)$. The resulting partial differential equation is the subject of the following three sections.

Before ending this section, we consider the case where the image plane $P1$ is located behind the write plane. This corresponds to a negative propagation length and we can exploit an interesting symmetry of the system. In fact our model is invariant under the following transformation:

$$\begin{aligned} L &\to -L \ , \\ \phi_{\max} &\to -\phi_{\max} \ , \\ E_{\text{in}} &\to E_{\text{in}}^* \ , \end{aligned} \tag{18}$$

where the second equation is replaced by $\mu_k \to -\mu_k$ in the Kerr approximation. The invariance described by (18) means that a negative propagation length corresponds to a change of the character of the nonlinearity, provided that an (inessential) operation of conjugation of the input field is performed. By using the same experimental setup, both cases of self-focusing and self-defocusing nonlinearities can be analyzed and compared with the model.

IV. STATIONARY AND HOMOGENEOUS STATES

In order to gain information about the system (5) and (15) [or (5) and (16) for the Kerr case], we first study the stationary and spatially homogeneous solutions $\phi^{(0)}$. By assuming a plane input wave and imposing $\frac{\partial}{\partial t} = \hat{\nabla}_\perp = 0$ one obtains the feedback intensity $I_f^{(0)}$:

$$I_f^{(0)} = \left(B^2 + C^2 + 2BC\cos\phi\right) I_{\text{in}} = \alpha\left(1 + \gamma\cos\phi\right) I_{\text{in}}, \tag{19}$$

with the following definitions:

$$\begin{aligned} \alpha &= B^2 + C^2 = \frac{1}{2}\left[\cos^2(\Psi_1 - \Psi_2) + \cos^2(\Psi_1 + \Psi_2)\right] \ , \\ \beta &= \frac{2B^2}{\alpha} = \frac{[\cos(\Psi_1 - \Psi_2) + \cos(\Psi_1 + \Psi_2)]^2}{\cos^2(\Psi_1 - \Psi_2) + \cos^2(\Psi_1 + \Psi_2)} \ , \\ \gamma &= \frac{2BC}{\alpha} = \frac{\cos^2(\Psi_1 - \Psi_2) - \cos^2(\Psi_1 + \Psi_2)}{\cos^2(\Psi_1 - \Psi_2) + \cos^2(\Psi_1 + \Psi_2)} \ . \end{aligned} \tag{20}$$

Here γ describes the amount of polarization modulation set by the polarization angles and α the linear losses which depend on the given configuration. Any additional loss in the feedback loop, e.g., leakage through the second beam splitter shown in Fig. 2, can be transferred directly into an effective value of the input intensity. For the saturation case one obtains

$$\phi^{(0)} = \begin{cases} \phi_{\max} & \text{for } (\mu_s I_f + J_b) < 0 \\ \phi_{\max}\left\{1 - \tanh^2\left[\alpha(1+\gamma\cos\phi^{(0)})\mu_s I_{\text{in}} + J_b\right]\right\} & \text{for } (\mu_s I_f + J_b) \geq 0 \ , \end{cases} \tag{21}$$

while for the Kerr approximation

$$\phi^{(0)} = \mu_k I_f^{(0)} + \phi_0 = \alpha\left(1 + \gamma\cos\phi^{(0)}\right)\mu_k I_{\text{in}} + \phi_0 \ . \tag{22}$$

The corresponding plots of $\phi^{(0)}$ versus the input intensity are shown in Fig. 5. The system shows optical multistability except for the case of pure phase modulation ($\Psi_1 = \Psi_2 = 0$, i.e., $\gamma = 0$). The form of the curves changes with the parameter J_b to the extent that the first hysteresis loop can degenerate into differential gain. The width of all hysteresis loops critically depends on the polarization configuration. $\gamma = \pm 1$ corresponds to the maximum effect leading to the separation of the branches while for $\gamma = 0$ the multistability vanishes. Analogous plots for the approximated Kerr type nonlinearity contain similar features apart from the fact that there is no limit to the number of stable branches because of the absence of saturation. In the presence of saturation, the accessible range of the phase is restricted to $0 \leq \phi^{(0)} \leq \phi_{\max}$, and so the number of multistable states is limited. The multistable behavior of such a system is well known and has already been described and realized in experiments [25,38,39].

For certain critical values ϕ_{crit} of the phase, the feedback intensity I_f vanishes. For example, in the case of $\gamma = +1$, ϕ_{crit} is an integer multiple of 2π while for $\gamma = -1$, ϕ_{crit} is an odd integer multiple of π. Values of ϕ_{crit} correspond to discontinuities which separate disconnected branches (see Fig. 5) and provide a good guideline for the understanding of some of the system's properties. One can easily see that switching from a lower up to a higher order branch roughly takes place for $\phi \simeq \phi_{\text{crit}}$ while the down switching happens at $\phi \simeq \phi_{\text{crit}} - \pi$. Correspondingly, the system can be initially positioned on a critical state $\phi(I_{\text{in}} = 0) = \phi_{\text{crit}}$ by setting

$$J_{b\text{crit}} = \operatorname{arctanh}(\sqrt{1 - \phi_{\text{crit}}/\phi_{\max}}). \tag{23}$$

For $\psi_1 = -\psi_2 = 45°$ (i.e., $\gamma = -1$) and $\phi_{\max} = 5\pi$ we find $J_{b\text{crit}}(\phi = 2\pi) = 1.0317$ and $J_{b\text{crit}}(\phi = 4\pi) = 0.4812$. As will be seen later on, these situations turn out to mark a drastic change in the stability properties of the system and therefore provide a good characterization of the system even for a weaker degree of polarization modulation. Optical multistability is also observed in nonlinear interferometers [40], e.g., in resonators containing a dispersive nonlinear medium. There, however, the case of the disconnected branches corresponds to a resonator with infinite finesse.

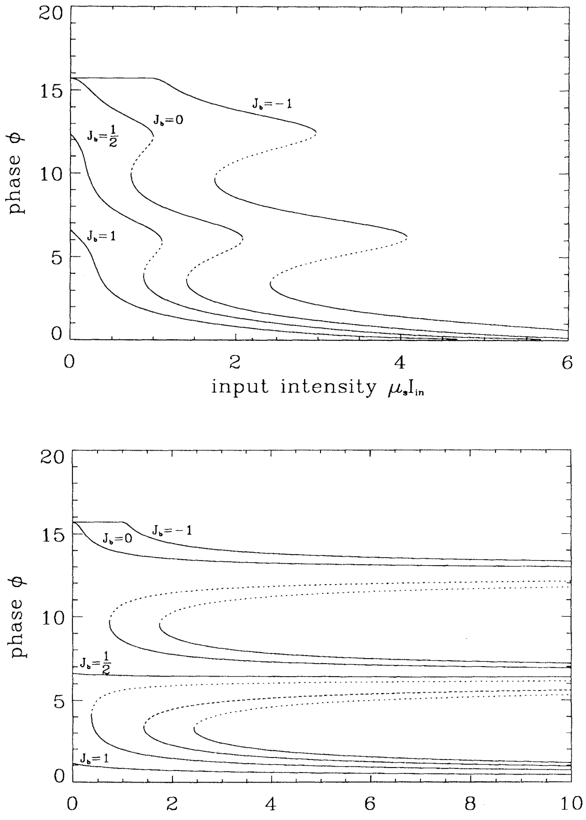

FIG. 5. Multistable stationary, homogeneous solution after the inclusion of saturation for different values of the bias intensity J_b. Upper plot: $\psi_1 = -\psi_2 = 22.5°$; lower plot: $\psi_1 = -\psi_2 = 45°$. Negative slopes are due to the defocusing type of nonlinearity, $\phi_{\max} = 5\pi$, $\hat{l} = 0.2$.

The sign of the nonlinearity (focusing-defocusing) does not play any peculiar role on the stationary states as the corresponding intensity transfer functions $I_f^{(0)}(I_{\text{in}})$ do not depend on either the sign of $\phi_{\max}$ or the sign of μ_k. The main difference between the saturation and the Kerr cases is that in the former there is a limitation of the phase range ($0 \leq \phi \leq \phi_{\max}$) so that the number of multistable branches is also limited.

Apart from the internal threshold, the final nonlinearity is determined both by the polarization configuration and the saturation. The setting of the polarization angles is mainly described by the parameter $\gamma(\psi_1, \psi_2)$, while for the saturation $\phi_{\max}$ and J_b are the most important parameters. Usually the selection of a certain LCLV apparatus and of a specific regime of operation fixes $\phi_{\max}$ and the polarization angles while J_b remains easily accessible by the external supply voltage. For these reasons, we will concentrate on the variation of J_b in the following.

V. LINEAR STABILITY ANALYSIS

As soon as diffraction is taken into consideration ($L \neq 0$), spatial instabilities occur, leading to the breakup of the homogeneous solutions and resulting in pattern formation. A standard method to determine the threshold for this behavior is the linear stability analysis. We add a small, time and space dependent perturbation to the homogeneous solution of the preceding section:

$$\phi = \phi^{(0)} + \varphi(x, y, t), \quad \text{with } \|\varphi\| \ll \phi^{(0)} \tag{24}$$

and impose the following conditions:

$$\tau \frac{\partial}{\partial t} \varphi = \lambda \varphi, \quad \hat{\nabla}_\perp^2 \varphi = -\hat{q}^2 \varphi, \tag{25}$$

where $\hat{q} = q\sqrt{L/2k}$ is an unscaled transverse wave number. Note that while the spatial condition of (25) in Cartesian coordinates leads to a sinelike spatial dependence, Bessel functions are a solution in polar coordinates, allowing for a separate (yet equivalent) interpretation of the stability analysis. Whenever the exponent λ is larger than zero, the perturbation grows exponentially and breaks up the stationary, homogeneous solution.

Inserting (24) and (25) into (5) and (15) [or (16) for the Kerr case], we obtain for the saturation case

$$\lambda = \frac{-2\phi^{(0)}\left[\beta\sin(\hat{q}^2)+\gamma\sin(\hat{q}^2-\phi^{(0)})\right]}{1+\gamma\cos\phi^{(0)}}\sqrt{1-\frac{\phi^{(0)}}{\phi_{\max}}} \times\left(\operatorname{arctanh}\sqrt{1-\frac{\phi^{(0)}}{\phi_{\max}}}-J_b\right)-\hat{l}^2\hat{q}^2-1 \qquad (26)$$

and

$$\lambda = \frac{(\phi^{(0)}-\phi_0)\left[\beta\sin(\hat{q}^2)+\gamma\sin(\hat{q}^2-\phi^{(0)})\right]}{1+\gamma\cos\phi^{(0)}} -\hat{l}^2\hat{q}^2-1 \qquad (27)$$

for the Kerr case. In both cases only the first term on the right-hand side can be positive, which means that diffraction is the cause of the spatial instability. The only role of diffusion, the other spatial coupling process involved in the LCLV system, is to damp higher spatial frequencies ($\lambda \sim -\hat{l}^2\hat{q}^2$) and therefore to stabilize the spatial structures.

The boundaries between stable and unstable parameter regimes are plotted in Figs. 6 and 7 by keeping Ψ_1, Ψ_2, l, J_b, and $\phi_{\max}$ (or ϕ_0 for the Kerr case) constant. Note that we consider a finite value of $\hat{l} = l\sqrt{2k/L} = 0.2$ as diffusion is always present in real experiments. Unstable regimes for $\hat{q} = 0$ correspond to the unstable branches of the stationary, homogeneous solutions (see Fig. 5). The horizontal lines, which have the most prominent effects for the case of $|\gamma| = 1$, correspond to the critical values of the phase ϕ_{crit}, as discussed above in Sec. IV. Figure 8 illustrates how an increasing parameter γ, i.e., the amount of polarization modulation, deforms the shape of the stability curves.

A natural choice of the control parameter would be the input pump intensity I_{in}. However, because of the multivalued nature of the relation between I_{in} and $\phi^{(0)}$, the stability curves plotted versus I_{in} are complex, folded, and then difficult to interpret. Since there is a continuous, monotonous relation between the induced phase and the pump intensity in each individual stable branch, the threshold of the instability corresponds, in general, to the lowest minimum of the stability curves $\phi^{(0)}(\hat{q}, \lambda = 0)$ versus $\hat{q}$. We will see later that there is one exception to this rule where the threshold is found in correspondence of a local maximum. The lowest possible unstable wave number is always favored because of the role played by the diffusion which damps higher spatial frequencies (their local minima showing then a higher threshold).

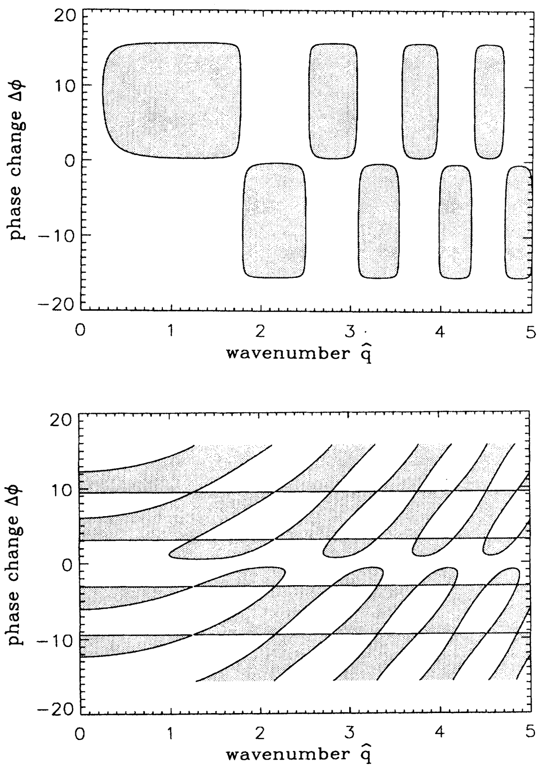

FIG. 6. Boundaries between stable and unstable (gray shaded areas) regimes for $\lambda = 0$ including saturation for pure phase modulation $\psi_1 = \psi_2 = 0$ (upper plot) and maximum polarization modulation $\psi_1 = -\psi_2 = 45°$ (lower plot), $J_b = 0$ in both cases. Self-focusing (positive phase change $\Delta\phi = \phi^{(0)} - \phi_{\max} > 0$) and self-defocusing (negative phase $\Delta\phi = \phi^{(0)} - \phi_{\max} < 0$) nonlinearity are included in each plot.

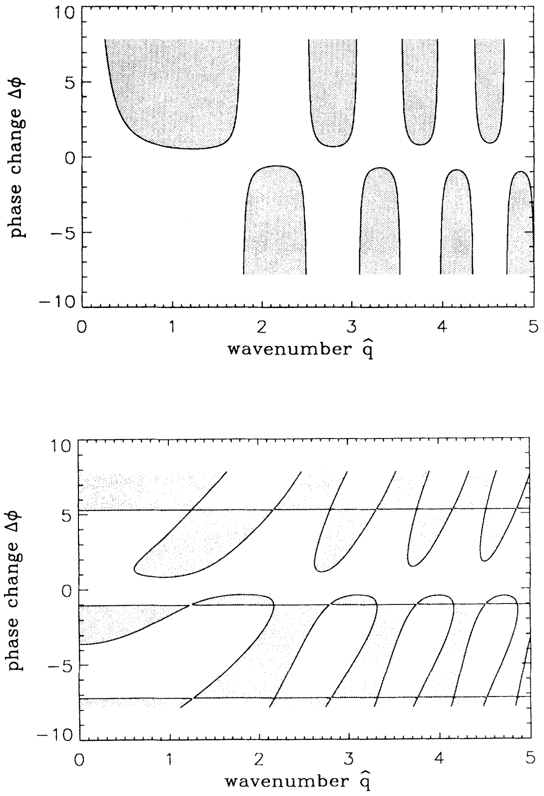

FIG. 7. Boundaries between stable and unstable (gray shaded areas) regimes for $\lambda = 0$ in the case of Kerr approximation for pure phase modulation $\psi_1 = \psi_2 = 0$ (upper plot) and maximum polarization modulation $\psi_1 = -\psi_2 = 45°$ (lower plot), $\phi_0 = 0$ in both cases. Self-focusing (positive phase change $\Delta\phi = \phi^{(0)} - \phi_{\max} > 0$) and self-defocusing (negative phase change $\Delta\phi = \phi^{(0)} - \phi_{\max} < 0$) nonlinearity are included in each plot.

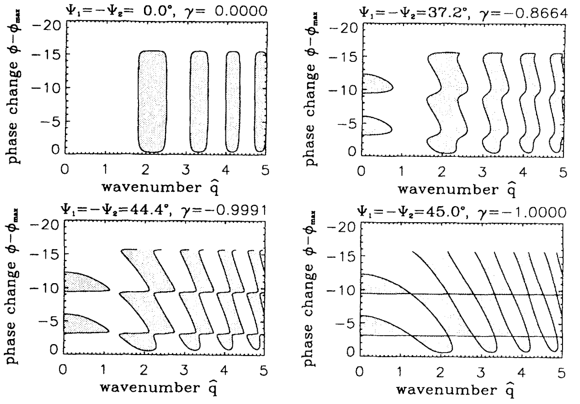

FIG. 8. Progressive modifications of the stability curves by varying the polarization modulation for the defocusing case with $J_b = 0$.

The threshold can be found as the local minimum of $\phi(\hat{q}^2)|_{\lambda=0}$, i.e.,

$$d\lambda = \frac{\partial \lambda}{\partial(\hat{q}^2)} d(\hat{q}^2) + \frac{\partial \lambda}{\partial \phi} d\phi = 0 \tag{28}$$

that can be rewritten as

$$\frac{\partial \phi}{\partial(\hat{q}^2)} = \frac{\partial \lambda}{\partial(\hat{q}^2)} \Big/ \frac{\partial \lambda}{\partial \phi}\bigg|_{\lambda=0} = 0 \ . \tag{29}$$

For the case including saturation we obtain

$$\begin{aligned} \frac{\partial \lambda}{\partial(\hat{q}^2)} &= \frac{-2\phi^{(}0)\left[\beta\cos(\hat{q}^2) + \gamma\cos(\hat{q}^2 - \phi^{(0)})\right]}{1 + \gamma\cos\phi^{(0)}} \\ &\quad \times \sqrt{1 - \frac{\phi^{(0)}}{\phi_{\max}}} \\ &\quad \times \left(\operatorname{arctanh}\sqrt{1 - \frac{\phi^{(0)}}{\phi_{\max}}} - J_b\right) - \hat{l}^2 \\ &= 0 \end{aligned} \tag{30}$$

while for the Kerr case the threshold corresponds to

$$\begin{aligned} \frac{\partial \lambda}{\partial(\hat{q}^2)} &= \frac{(\phi^{(0)} - \phi_0)\left[\beta\cos(\hat{q}^2) + \gamma\cos(\hat{q}^2 - \phi^{(0)})\right]}{1 + \gamma\cos\phi^{(0)}} - \hat{l}^2 \\ &= 0 \ . \end{aligned} \tag{31}$$

It is important to note that in some instances a homogeneous ($\hat{q} = 0$) instability corresponds to the lowest threshold.

Unfortunately it is not possible to express the threshold conditions (26) and (30) [(27) and (31) for the Kerr approximation] in an explicit way, except for one special case. For vanishing diffusion ($l \simeq 0$) and pure phase modulation ($\gamma = 0$) we recover in the Kerr approximation the following threshold conditions:

$$\begin{aligned} |\mu_k| I_{\text{inth}} &= \frac{1}{2}, \quad \hat{q}^2_{\text{th}} = \frac{\pi}{2} \quad \text{for } \mu_k > 0, \\ \hat{q}^2_{\text{th}} &= \frac{3\pi}{2} \quad \text{for } \mu_k < 0, \end{aligned} \tag{32}$$

which corresponds to the result given by D'Alessandro and Firth for the single-feedback Kerr slice [18–20].

For all other cases it is necessary to use a Newton algorithm to numerically determine the threshold values $\hat{q}_{\text{th}}$ and I_{inth}. These are shown in Fig. 9 for a range of the bias intensity J_b in the saturation case. The graphs for the Kerr case show very similar features and are then omitted. Note that the implicit nature of the threshold equations makes analytical studies of the stability of patterns above threshold an almost impossible task. For example, the weakly nonlinear analysis suggested in [20] can only be implemented by coupling several numerical methods with obvious difficulties of convergence of the algorithms. Only specific patterns arising in limited domains of the parameter space can be studied in this way, further reducing the relevance of this complex technique

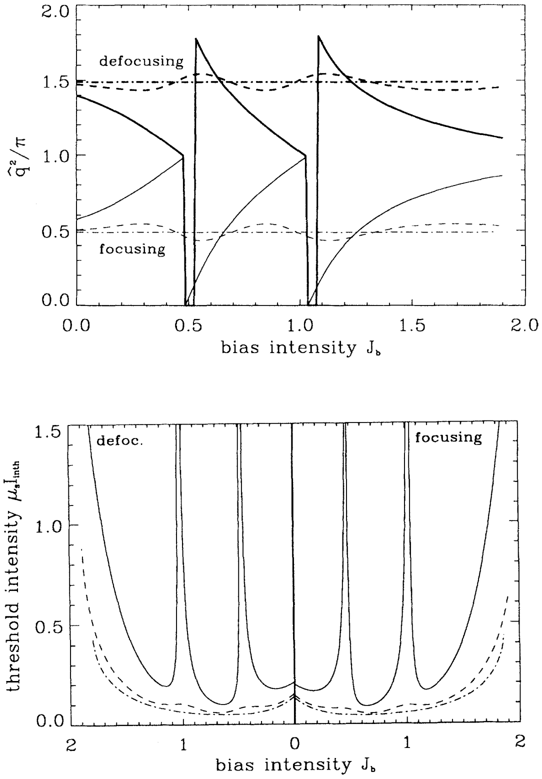

FIG. 9. Pattern forming threshold for focusing and defocusing nonlinearities, and three polarization configurations $\psi_1 = -\psi_2 = 45°$ (solid line), $\psi_1 = -\psi_2 = 22.5°$ (dashed line), and $\psi_1 = -\psi_2 = 0°$ (dash-dotted line). The upper plot shows the square of the unstable wave number at threshold q^2_{th} versus J_b. The lower plot shows the threshold pump intensity $\mu_s I_{\text{inth}}$ versus J_b. In the lower plot, focusing and defocusing cases are presented in the left and right part of the figure, respectively.

in a broad overview of the main features of our model. For these reasons, the stability analysis of patterns above threshold is omitted here.

For pure phase modulation, both $\hat{q}_{\rm th}$ and $I_{\rm inth}$ do not change with J_b. With the inclusion of polarization modulation ($\gamma \neq 0$), however, the unstable wave number $\hat{q}_{\rm th}$ presents a dependence on J_b. For maximum polarization modulation (i.e., $\Psi_1 = -\Psi_2 = 45°$; $\gamma = -1$), the unstable wave number varies between zero and $\sqrt{\pi}$ for the focusing case and between $\sqrt{\pi}$ and $\sqrt{2\pi}$ for the defocusing case. In other words, the typical pattern length scale can easily be adjusted by the external supply voltage of the LCLV for a fixed diffraction length. The fee of this interesting feature is that the pump threshold also depends on J_b. In particular for critical values $J_{b\rm crit}$ of the bias intensity [see Eq. (23)] the pump threshold may diverge.

A rough estimate of the minimum pump threshold is obtained by the condition of $\hat{q}_{\rm th}$ equal to the constant value of the pure phase modulation case. For values of J_b around 2, the pump threshold diverges as the system is driven into saturation. As was already seen for the single-feedback Kerr slice, the corresponding unstable wave numbers for the focusing and the defocusing case are separated by $\sqrt{\pi}$; self-defocusing patterns always show a smaller length scale.

If the diffraction length L is set to zero in our system, pattern formation is in general avoided as the typical pattern length scale $\Lambda = 2\pi/q \sim \sqrt{L}/\hat{q}_{\rm th}$ tends to zero. Patterns are then suppressed by diffusion and/or the limited spatial resolution of the system. In the present case, we observe very small or even vanishing values of $\hat{q}_{\rm th} \to 0$, which can balance the above effect. Even for very small diffraction lengths L, patterns with finite length scale can still emerge. This can be relevant for practical applications, where it is often desirable to avoid pattern formation in order to use other features of the system (e.g., the multistability for parallel optical memory). Since the slightest defocusing of the imaging of the read-out beam onto the write side of the LCLV introduces diffraction, the LCLV setup easily produces spatial instabilities even in cases of careful adjustment of the optics.

Discontinuities of the unstable wave number and of the pump threshold appear for the critical values of $J_{b\rm crit}$ [see Eq. (23)]. This can easily be understood from the change of the shape of the stability curves near critical points, as shown in Fig. 10 for a defocusing medium, and in Fig. 11 for the focusing case. These graphs also illustrate the shift of the first minimum which determines the unstable wave number $\hat{q}_{\rm th}$ for a given J_b. Furthermore one can see that in the defocusing case the local minimum near $\hat{q} = 2.5$ competes with an unstable regime at $\hat{q} = 0$ corresponding to a homogeneous instability, shortly after crossing a critical point. Since higher $\hat{q}$'s are damped by diffusion, the homogeneous instability can survive within a short interval of values of J_b, until a jump to a finite value of $\hat{q}$ (see Fig. 9). Note also that in this case the stability curves are very flat so that instead of a well-defined unstable wave number a whole range of wave numbers participates in the formation of the pattern.

For the focusing case, such a competition does not take place since near $J_b \simeq J_{b\rm crit}$ the homogeneous and inhomogeneous instabilities coincide. However, in the experimentally relevant case of finite pump beam waists, this competition may still take place. The limited beam size can suppress any patterns with very low (or vanishing) wave numbers. Therefore the closest higher order wave number belonging to the next lowest local minimum of the stability curves (see Fig. 11) may come into play and force an inhomogeneous instability.

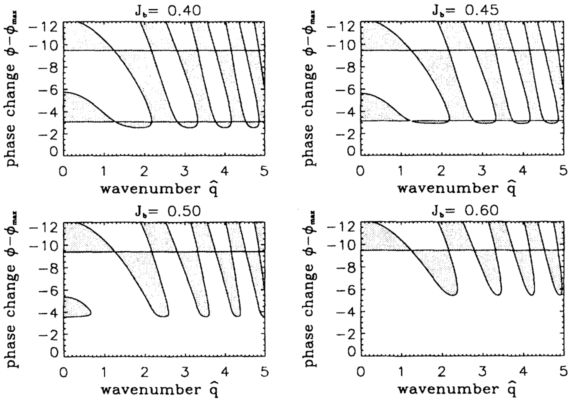

FIG. 10. Progressive modifications of the stability curves near the critical bias intensity J_b for the defocusing case.

The linear stability analysis cannot decide the outcome of the competition between homogeneous and inhomogeneous instabilities. In any case, it is important to study the coexistence of a stable, flat solution and a pattern forming solution because it can lead to the formation of the so-called "isolated states." These are single, independent spots, which do not necessarily arrange in geometrically ordered patterns [41–43].

The stability properties of the case including saturation fundamentally differ from the Kerr approximation in one particular instance. When the system is strongly driven into saturation, any perturbation of the feedback wave will no longer induce a corresponding change of the

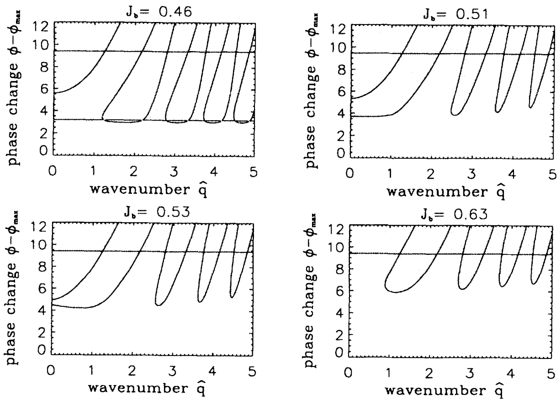

FIG. 11. Progressive modifications of the stability curves near the critical bias intensity J_b for the focusing case.

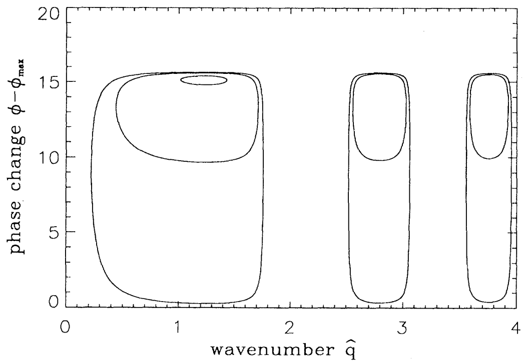

FIG. 12. Shrinking of the instability regimes with increasing J_b for a focusing nonlinearity and pure phase modulation $\psi_1 = \psi_2 = 0$. $J_b = 0.0$, 1.0, 1.8 from the largest to the smallest loops, respectively. The "lower" threshold corresponds to the lowest local minimum, the "upper" threshold to the highest local maximum.

phase and therefore will die out. The homogeneous state is stable for high saturations and correspondingly the stability curves are closed loops in Fig. 6 (in the case of maximum polarization modulation this feature does not appear in the graph since the upper limit is obtained at a critical phase value $\phi = \phi_{\text{crit}} = \phi_{\text{max}}$). From Fig. 12 one can also see how the size of the unstable regime shrinks with increasing bias intensity J_b, since the system comes closer to saturation. Here we are led to the interesting situation that it should be possible to overrun the pattern formation by driving the system into a homogeneous and saturated state. Vice versa, by *decreasing* the pump intensity from the homogeneously saturated state, one crosses a spatial instability that we label as "upper threshold" in contrast to the "lower threshold" for pattern formation obtained with increasing pump power.

Another interesting situation can be studied in this system. Setting J_b to a negative value corresponding to an operating point below the internal threshold, the pump intensity needs to attain a threshold value $\mu_s I_{\text{in}} = -J_b$ in order to induce a reaction in the LCLV [see Eq. (15)]. In this way, a high intensity light is present in the system before a modification of the refractive index takes place. An abrupt reaction of the system and a behavior that strongly depends on the "wake-up" condition $\phi(\mu_s I_{\text{in}} = -J_b) = \phi_{\text{max}}$ are observed. An example for $\phi_{\text{max}} = 5\pi$, $J_b = -5$, defocusing nonlinearity, and $\psi_1 = -\psi_2 = 45°$ is shown in Fig. 13. Again we are faced with a very flat stability curve leading to the participation of a wide band of wave numbers to the process of pattern formation close to threshold.

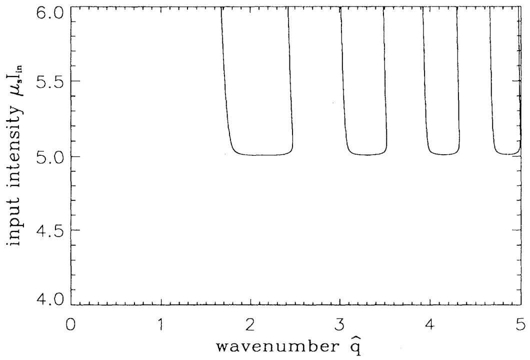

FIG. 13. Stability curves for operation below the LCLV's internal threshold with $J_b = -5$, defocusing case, and maximum polarization modulation $\psi_1 = -\psi_2 = 45°$.

VI. NUMERICAL SIMULATIONS

The results of the preceding section already display the richness of instabilities of the LCLV feedback system with the inclusion of polarization and saturation effects. In order to present a complete description of the behavior of the system, however, numerical simulations are necessary. In this section we provide a survey of the most interesting cases for plane wave pumping by selecting parameter values corresponding to the most representative situations.

The numerical computer code is a combination of finite difference and spectral methods. The diffusion equation is separated from the propagation and is integrated by using a hopscotch scheme [44]. This numerical method alternates an implicit and an explicit scheme on even and odd sublattices of the original grid (in general of 128×128 points). It has been already used successfully in the description of thin Kerr slices in front of a single mirror [19,20] and in other nonlinear optical systems. The propagation part is then solved exactly by a straightforward use of fast Fourier transform. The codes have been optimized to run efficiently on dedicated workstations. Transients have been discarded. All patterns shown in this section are images of the phase distribution in the plane transverse to the propagation, the feedback intensity distribution, in general, having the same transverse structure. Any constant bias of the phase is not shown in the images, so that the images represent the spatial phase variation only.

The main result of these simulations is the fact that the system under consideration presents a large variety of patterns. In particular, all "basic" patterns, such as rolls, squares, hexagons, and negative hexagons were observed. In Fig. 14 a selection of structures close to threshold is presented. They correspond to the same polarization configuration under a simple variation of the bias intensity J_b. Other typical results are shown in Fig. 15.

Close to threshold, stationary patterns are dominant. The term "close" depends on the parameter selection. In most cases, the asymptotic patterns are stationary for at least 10% above threshold. In some cases, however, we are not able to find regular and stationary patterns even for input intensities just 10^{-4} times above threshold. Other patterns show a complex order, constituted of small spots of different height which form complicated subpatterns on a larger hexagonal or even square lattice (see Fig. 14 for $J_b = 0.2$). Sometimes the whole pattern constantly moves as a rigid structure across the transverse plane. These complex patterns develop in general

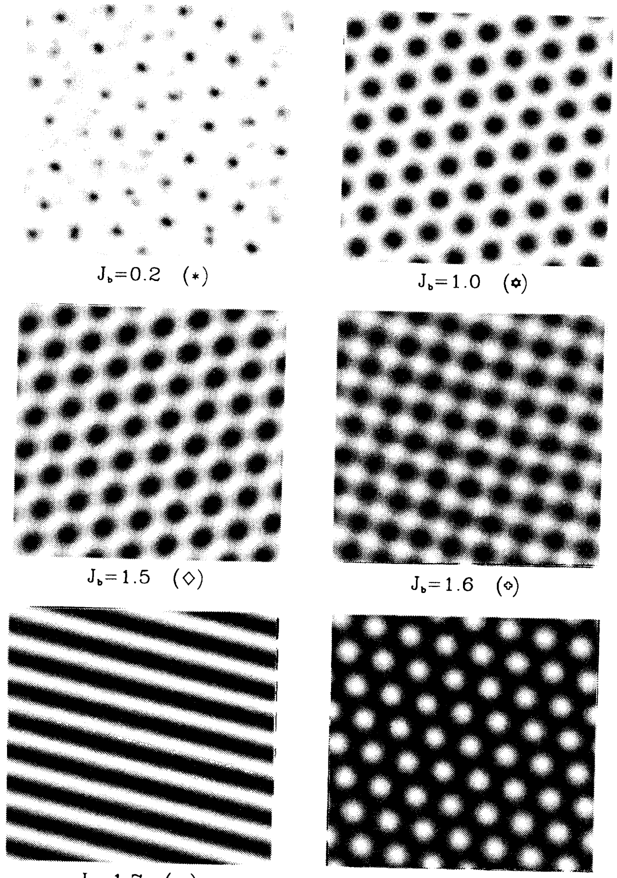

$J_b=0.2$ (*) $J_b=1.0$ (✡)
$J_b=1.5$ (◇) $J_b=1.6$ (✙)
$J_b=1.7$ (=) $J_b=1.8$ (*)

FIG. 14. Different types of patterns found for pure phase modulation $\psi_1 = \psi_2 = 0$ with a defocusing nonlinearity under the variation of J_b. Each square has sides of length 4.8 in normalized space units.

for small values of J_b, where the saturation function has a large curvature ($|\,\partial\phi/\partial I_{\rm in}\,|$). If the feedback intensity grows locally, the system experiences a higher sensitivity to local phase modulations. This effect can lead to a runaway process destabilizing the regular pattern immediately above threshold.

Regarding regular patterns, the transitions between hexagons and squares, and between squares and rolls, is mostly smooth under variations of J_b. Approaching the hexagon-square transition, for example, one of the three space directions in the hexagonal grid breaks the symmetry and starts to dominate (see Fig. 14 for $J_b = 1.5$) causing the hexagons to deform into a rhombic structure [as in Fig. 15(b)] until they finally reach a square pattern. Similarly, when one direction of the square lattice prevails, the spots start to merge until the formation of stable rolls. Rolls appear to be always related to squares, the latter often affecting the transients. Direct transitions between hexagons and rolls have not been observed. Roll patterns are often subjected to weak zigzag instabilities leading to a kind of "wavy" rolls, as shown in Fig. 15(a).

To get an overview of the dependence of the type of pattern on the main parameters $\gamma(\psi_1, \psi_2)$ which specifies the polarization configuration, and J_b which depends on the external voltage, a rough outline of the bifurcation diagram, in the vicinity of the threshold, is presented in Fig. 16. The symbols used to indicate the pattern type correspond to those introduced in Figs. 14 and 15. Note that the computation of these diagrams requires a considerable amount of CPU time. Some global features can be identified from this diagram: (a) The complex patterns mentioned above only appear for small values of J_b and more often in the self-defocusing case than in the focusing one; (b) hexagons dominate the regime of intermediate bias intensity J_b well above the LCLV's internal threshold but away from strong saturation. In particular, for focusing nonlinearities, hexagons persist on a broad range of the parameter space, while in the defocusing case other types of patterns might prevail. For strong modulations of the polarization (large values of ψ_1) and for both signs of the nonlinearity, the presence of patterns other than the hexagons increases. In particular, rolls appear and persist in the upper right corner of the diagram, i.e., for large polarization modulations and incipient saturations. As already mentioned, squares always appear between hexagons and rolls. Square structures develop from hexagons via a continuous deformation where rhombic structures are the intermediate step. It is therefore

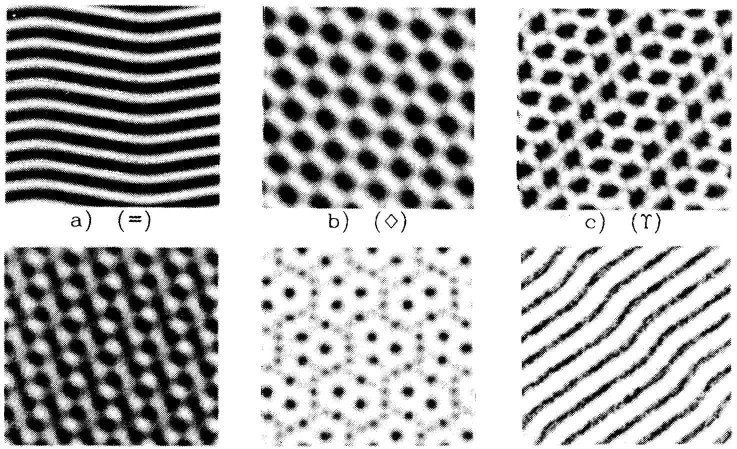

a) (=) b) (◇) c) (ϒ)
d) (*) e) (*) f)

FIG. 15. Samples of typical patterns obtained just above threshold: (a) rolls showing zigzag instability ("wavy" rolls) for $\psi_1 = -\psi_2 = 40°$, focusing case, $J_b = 1.5$, (b) rhombic structure for $\psi_1 = -\psi_2 = 45°$, defocusing case, $J_b = 1.5$, (c) partially ordered ragged spots for $\psi_1 = -\psi_2 = 45°$, defocusing case, $J_b = 1.05$, (d) complex ordered structure for $\psi_1 = -\psi_2 = 22.5°$, defocusing case, $J_b = 0.7$, 2.5% above threshold, (e) complex ordered structure for same parameters as (d), but 10% above threshold. (f) Roll pattern for negative bias intensity $J_b = -5$, $\psi_1 = -\psi_2 = 45°$, defocusing case. Each square has sides of length 4.8 in normalized space units.

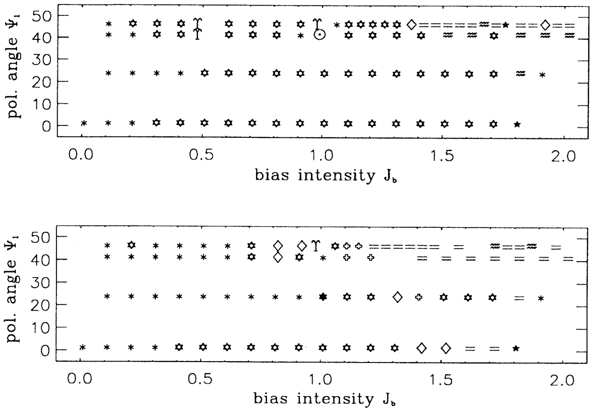

FIG. 16. Bifurcation diagram showing the type of pattern obtained close to threshold depending on the polarization configuration and the amount of saturation. $*$: complex structure, ✡: hexagons, $\star$: negative hexagons, $=$: rolls, $\approx$: "wavy" rolls, $\diamond$: rhombic structure, Υ: ragged, weakly disordered spots, $\odot$: isolated states.

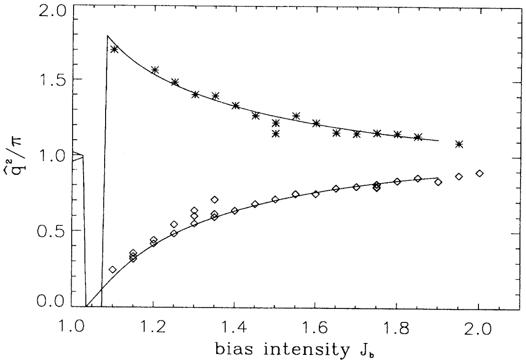

FIG. 17. Comparison of the wave numbers between the numerically found patterns and the theoretical estimate (solid line) for maximum polarization modulation $\psi_1 = -\psi_2 = 45°$.

somewhat arbitrary to draw the line between deformed hexagons and rhombic patterns.

In the vicinity of the critical values of $J_b(\phi_{\rm crit})$ of Eq. (23) and for large polarization modulation, we find a dynamical (weakly turbulent) state, in which spots and a reminiscent hexagonal lattice are still observable [see Fig. 15(c)]. In one case, evidence of the so-called "isolated states" has been found (see the end of this section for details). All the rare cases of negative hexagons belong to large values of the saturation.

Many different patterns are also found in the case of pure phase modulation. This is one of the main differences between our and the Kerr model for which phase-only modulation generates hexagons only [18–20]. One can then conclude that the nonlinearity introduced by the saturation function and controlled by J_b is responsible for the generation of different types of patterns. However, we note here that the addition of the nonlinearity caused by the polarization modulation also influences the pattern type and modifies the pattern scenarios.

Figure 17 shows the characteristic spatial wave number determined numerically in a comparison with the results of the linear stability analysis for the case of maximum polarization modulation. For the case of pure phase modulation ($\psi_1 = \psi_2 = 0$) the characteristic wave number is found to be insensitive to changes of J_b and to agree with the constant value predicted by the theory. Discrepancies between the numerical simulations and the results of the linear stability analysis are mainly due to the utilization of periodic boundary conditions, which have been chosen to approximate the plane pump wave. The complete translational symmetry of a plane wave, however, is not achievable since any regular pattern evolving and containing the transverse wave vectors $\vec{q}_i$ has also to satisfy the periodic boundary condition $\vec{q}_i = n(2\pi/A)\,\vec{e}_x + m(2\pi/A)\,\vec{e}_y$, where A is the linear size of the grid (note that this is very similar to the problem of x-ray diffraction in crystals). Only a discrete set of wavenumbers q_i is allowed, their density being higher the larger the number of grid points. In order to fit this constraint, patterns can rotate without modifying their characteristic wave number. For further matching, the value of the wave number shifts, causing small discrepancies between theory and simulations.

In the presence of rolls, only one wave number is obtained from the computed images. Squares were never found to deform to rectangles via the slight shift of the wavelengths in the two independent directions. Hexagons, however, do often deform to adapt to the periodic boundaries. In this way, two, sometimes three slightly differing wave numbers were found for each hexagonal configuration (see Fig. 17). It is interesting to note that at least one of these wave numbers always matches the theoretical value almost exactly. Moreover, simulations on larger lattices have shown the discrepancies to vanish.

As stated in the preceding section, pattern formation can be overrun by driving the system into saturation. As an example, we have chosen a self-defocusing nonlinearity and the following parameters: $\psi_1 = -\psi_2 = 22.5°$

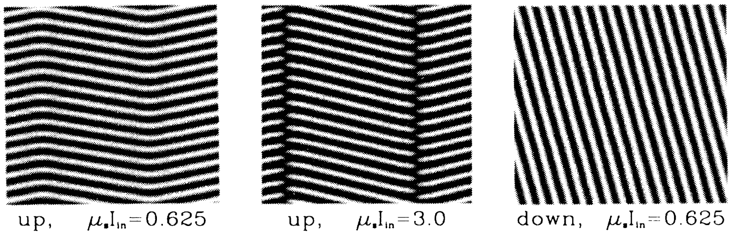
up, $\mu_{\bullet}I_{\rm in}=0.625$ up, $\mu_{\bullet}I_{\rm in}=3.0$ down, $\mu_{\bullet}I_{\rm in}=0.625$

FIG. 18. Examples of patterns developing while overrunning the unstable regime for increasing (up) and decreasing (down) pump, intensity as indicated. Each square has sides of length 9.6 in normalized space units.

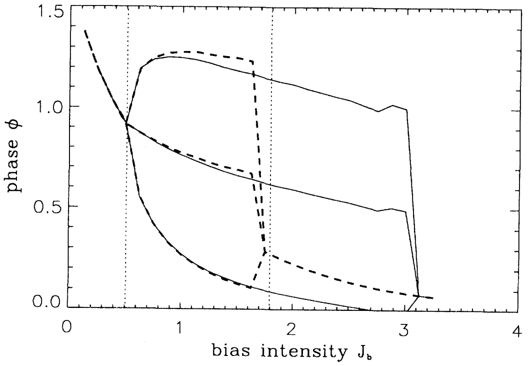

FIG. 19. Changes of the average phase and deviation from average phase versus the increasing (solid line) or decreasing (dashed line) bias intensity J_b. Vertical lines show the position of the theoretical lower and upper thresholds.

and $J_b = 1.8$. In this set of simulations, the pump intensity was increased in steps from below threshold until saturation was reached, and then reversed. It was indeed possible to reach a homogeneous saturated state. Moreover, the existence of an "upper" threshold for pattern formation (see Fig. 12) obtained by *decreasing* the pump intensity, has been confirmed. Typical patterns observed in these simulations are shown in Fig. 18. We find that the evolution of rolls undergoes a pronounced zigzag instability. Shortly before their collapse into the homogeneous, saturated state, rolls break transversally and form a herringbone kind of pattern. Note that when decreasing the pump intensity, only straight rolls have been observed.

In order to detect the onset of pattern formation in these simulations, we have evaluated the standard deviation of the phase taken over the whole image. In Fig. 19 the average of the phase is plotted versus the pump intensity together with the positive and negative deviations from such a value. The onset and collapse of pattern formation can be easily identified by the abrupt change of the standard deviation. In this plot the theoretical values of the "lower" and "upper" thresholds are also reported and they turn out to be in good agreement with the numerical simulations. An interesting bistability between a pattern and a homogeneous state exists just above the upper threshold value (second dashed vertical line in Fig. 19). The pattern, once established by increasing the pump intensity, survives far above the upper threshold into the regime of saturation. This behavior might be related to the fact that robust rolls are expected to develop in this region of the parameter space. Things might be different in regimes where hexagons or squares develop.

As long as saturation is involved, pattern formation is observable in a limited interval of the pump intensity (i.e., between the lower threshold and strong saturation). Again, this is not the case for a Kerr-type nonlinearity. In the latter case, as in many other nonlinear optical systems, dynamic and possibly disordered ("turbulent") states often arise from stationary and regular patterns under the action of strong pumps. We briefly discuss here two examples of intensity patterns far above threshold for self-focusing nonlinearity and maximum polarization modulation $\psi_1 = -\psi_2 = 45°$ (see Fig. 20). In the first case, the stationary pattern close to threshold is hexagonal (see lower part of Fig. 20). By increasing the pump, the spots become ragged and begin to jitter around their lattice sites. Then spots start to merge, new spots appear, the hexagonal order breaks down, and the pattern becomes more and more dynamical. Nevertheless, for very high intensities, the hexagonal order is reestablished. The breakdown and reappearance of the hexagonal order appears to be a discontinuous process, since intermediate ordered states have been observed as well. These findings could be compared to experimental observations done for a similar system [16].

The second case investigated here corresponds to the same parameters but uses a higher value of the bias intensity (see upper part of Fig. 20). We start from rolls undergoing a zigzag instability. Eventually, the rolls start to fragment into negative spots (dips instead of peaks) forming patches on a rhombic pattern. In this sequence almost no dynamics takes place, apart from a very slow motion of the rolls (spots). Putting this together with the findings obtained for the patterns of Fig. 18, one could conclude that rolls are more robust than hexagons in LCLV feedback systems.

Another feature apparent from the images of Fig. 20, is that the typical length scale decreases with increasing pump (up to ~ 20% for the rolls, and ~ 30% for

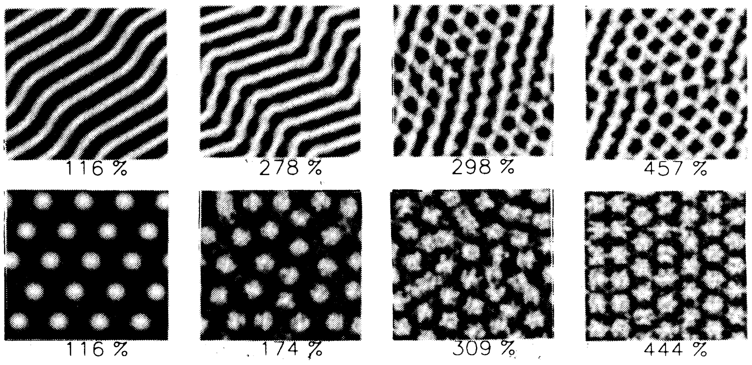

FIG. 20. Samples of patterns obtained for input intensities far above threshold, focusing nonlinearity, $\psi_1 = -\psi_2 = 45°$, $J_b = 1.6$ (upper) and $J_b = 1.1$ (lower). Percentages of the pump intensities relative to the corresponding threshold values are also indicated. Each square has sides of length 6.4 in normalized space units.

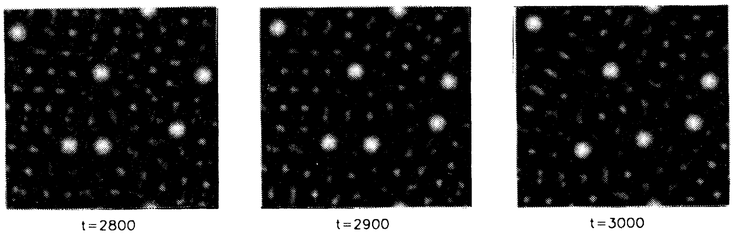

FIG. 21. Temporal sequence of wandering isolated states for focusing nonlinearity, $\psi_1 = -\psi_2 = 40°$, $J_b = 1.0$, and just above threshold. Time is shown in units of τ. Each square has sides of length 8.8 in normalized space units.

the hexagons). This is in good agreement with the fact that the stability curves, in the case of polarization modulation, bend towards higher spatial frequencies above threshold for the self-focusing case (see Fig. 6, lower plot). Note that this result of the *linear* stability analysis holds far above threshold as well.

In the preceding section, the possibility of finding isolated states in our system has been mentioned. Numerical evidence corroborates our claim. In Fig. 21 samples of the temporal evolution of the transverse phase distribution are shown for an evolution close to threshold, a self-focusing nonlinearity, and a polarization configuration of $\psi_1 = -\psi_2 = 40°$. The threshold conditions are roughly comparable to the ones shown in the lower plot of Fig. 10; a very low unstable wave number (a reminiscence of a homogeneous instability) coexists with a larger wave number. In this sequence we observe individual spots, slowly moving in the transverse plane. Two spots appear to merge when their distance is smaller than a critical value and repel at larger distances, suggesting the presence of long-range interactions. The sequence presented in Fig. 21 has been found just above threshold where dynamical evolutions are more common. We aim to further investigate localized states in future work and in particular to study the possibility of controlling the formation of individual spots.

Finally, one example of operation below the LCLV's internal threshold ($J_b < 0$) is presented. In the case of a defocusing nonlinearity, $\psi_1 = -\psi_2 = 45°$ and $J_b = -5$, we observed the formation of "wavy" rolls, as shown in Fig. 15 (f). In contrast to previously described rolls (for positive values of J_b), these rolls are noisy and have a fuzzy profile. This is in agreement with the theoretical finding that in such a case a whole band of spatial frequencies becomes unstable (see Fig. 13).

VII. EXPERIMENTS

In this section we present experimental results that test the reliability of our theoretical and numerical predictions. A setup similar to the configuration presented in Fig. 22 has already been used to investigate pattern formation in presence of pure phase modulation [12,16]. We have modified it to include polarization effects. Since the phenomena described in the preceding sections are most pronounced in the case of maximum polarization modulation, the angles of the input polarization and of the polarizer have correspondingly been set around $\psi_1 = 45°$ and $\psi_2 = -45°$. Nevertheless, the last paragraph of this section describes a roll-hexagon transition due to saturation effects in the pure phase modulation case to stress the differences with the Kerr approximation.

Figure 22 shows the experimental configuration: a linearly polarized HeNe laser is used as light source for the pump wave and operates at 633 nm with an output power of 10 mW. An acousto-optical modulator (AOM) is then used to control the pump beam intensity, which is monitored by a photodiode (PD). The light beam is then expanded so that only its central part is used as input in order to achieve a pump profile as flat as possible.

The feedback loop is set up by the first beam splitter BS1, the prisms $M1$, $M2$, which act as mirrors, the polarizing beam splitter BS2, and the mirror $M3$. The lenses $L1$ and $L2$ form a confocal configuration and image the

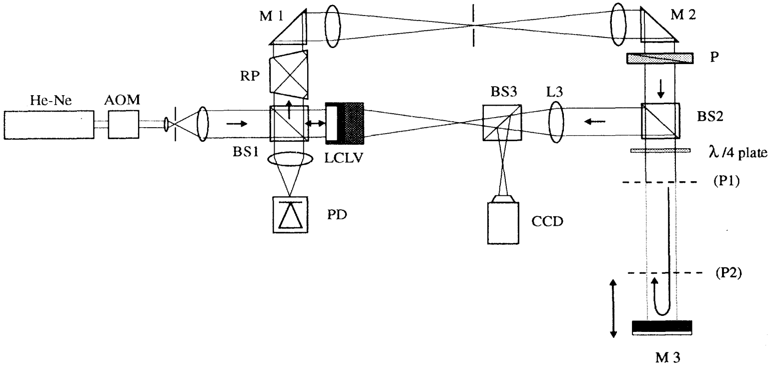

FIG. 22. Scheme of the experimental setup. Details are provided in the text.

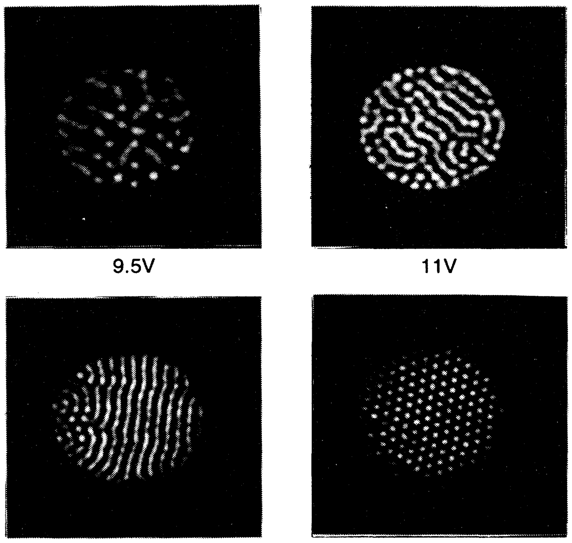

9.5V 11V

13V 13.8V

FIG. 23. Examples of experimentally found patterns for the focusing case and values of the external voltage V_{ext} as indicated. The visible beam diameter is 6 mm.

LCLV output plane onto the plane $P1$. After leaving this plane, the feedback wave freely propagates until reaching the plane $P2$, which is the object plane of the lens $L3$. This lens images the light distribution at $P2$ onto the write side of the LCLV. In this way diffraction effectively takes place between $P1$ and $P2$ only. The mirror $M3$ is mounted on a computer-controlled slit, allowing for simple and precise control of the diffraction length L. If the object plane $P2$ is put in front of $P1$, we can experimentally simulate a self-focusing nonlinearity [28], without changing the setup (see discussion above). BS2 is a polarizing beam splitter that in combination with the $\lambda/4$ retarder plate directs all the light coming from $M2$ to the LCLV write side.

The feedback wave undergoes many reflections at the mirrors while propagating through the feedback loop. In a misaligned setup, any light distribution entering the feedback loop from the LCLV read-out side would not only be shifted when reaching the write side, but also rotated. To facilitate the adjustment of the setup, which requires simultaneous elimination of the shift and the rotation, a rotating prism (RP) is utilized, allowing for final compensation of any remaining rotation. The properly aligned setup is translationally (apart from the pump beam profile) and rotationally symmetric with respect to the feedback wave propagation direction.

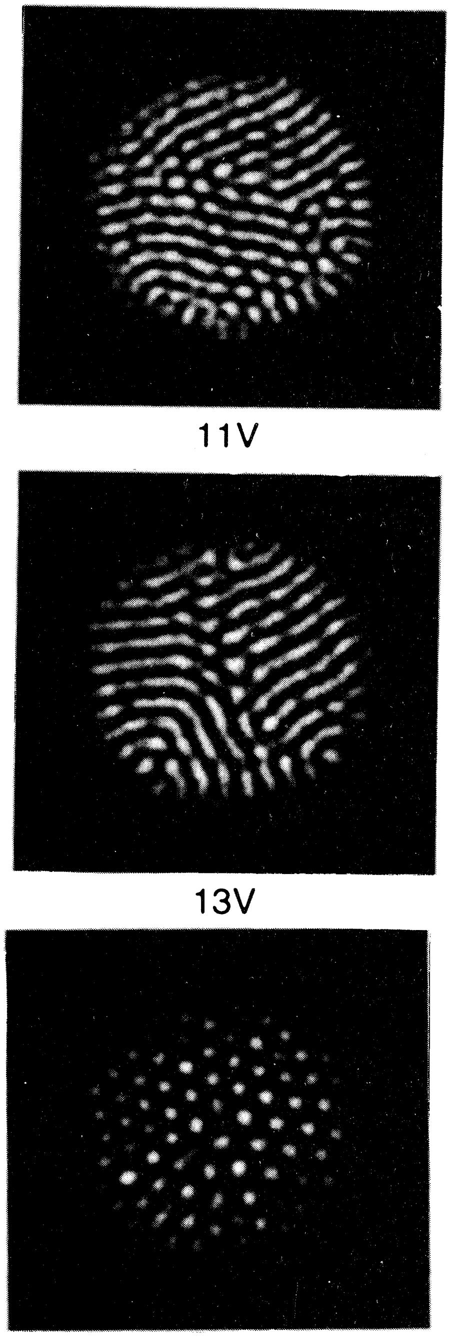

11V

13V

13.8V

FIG. 24. Examples of experimentally found patterns for the defocusing case and values of the external voltage V_{ext} as indicated. The visible beam diameter is 8 mm.

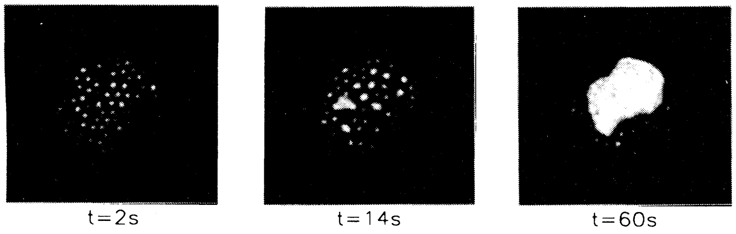

t=2s t=14s t=60s

FIG. 25. Transient evolution towards a homogeneous state of an experimental hexagonal pattern (defocusing case, $V_{\text{ext}} = 13.92$ V). The visible beam diameter is 6 mm.

Together with the lenses $L1$ and $L2$, the pinhole PH forms a spatial low-pass filter, which controls the spatial resolution of the system. Consequently, the effective diffusion length can be selected within a reasonably wide range. In the present case it has been evaluated at $l = 80\ \mu$m. With an effective pump beam diameter of 6 mm, our system reaches a resolution of 75 lines in each transverse dimension. On one hand one would like to achieve a very large aspect ratio for a comparison with the theoretical and numerical predictions. On the other, we avoid moving too close to the limit imposed by the spatial resolution and select a ratio of pattern length scale over aperture diameter Λ/A around $10-20$, a reasonable compromise. As already discussed, the typical pattern scale $\Lambda = \sqrt{L/2k} \times 2\pi/\hat{q}$ differs between the self-focusing and self-defocusing nonlinearities. Different propagation lengths of $L_{\rm sf} = 12$ cm for the focusing and $L_{\rm sdf} = 44$ cm for the defocusing case have then been chosen.

A charge-coupled device (CCD) camera, connected to a video cassette recorder and a PC-based image processing system, detects the feedback wave. The camera can be positioned to detect either the intensity distribution in the write plane of the LCLV or the corresponding spatial Fourier spectrum in the focal plane of $L3$. The latter is used to determine the dominant transverse wave number. The spectrum was scaled by introducing a transmission grating of known grating constant into the feedback loop.

Typical examples of stable patterns found for the focusing case are shown in Fig. 23, and in Fig. 24 for the defocusing case. Clearly the formation of rolls and hexagons can be identified. Differently from hexagons, rolls cannot fit well into the circular boundary and a competition of different orientations is observed. Similar roll patterns have previously been observed in [14], but have been ascribed to misalignments or aberrations of the setup. Here we demonstrate that these patterns are a generic feature of the coupling between diffraction and polarization modulation and cannot be eliminated by simple adjustment of the optics. Together with regular arrangements of hexagons, patterns are often affected by defects. Clear square patterns have not yet been observed. On one side, numerical simulations show that their range of existence is rather small. On the other hand, it is still unclear how robust square patterns are and if they would survive under the effects of a limited aspect ratio and circular boundaries. The pattern corresponding to $V_{\rm ext} = 9.5$ V in the focusing case (see Fig. 23) partially reminds one of the numerically obtained patterns displayed in Fig. 21, where uncorrelated and isolated spots appear to exist. In the defocusing case a competition between an inhomogeneous and a homogeneous state is observed. Hexagonally arranged spots change their size and begin to merge (see Fig. 25) and finally a global switching to a homogeneous state takes place. This is experimental evidence that a flat state, related to an upper branch of the multistable plane wave solution (cf. Fig. 5) can coexist with patterns. A systematic experimental investigation of pattern formation and competition is planned to be the subject of future work.

In Fig. 26 a comparison between the experimentally found dominant transverse wave number and theoretical curves is presented and shows good agreement. There

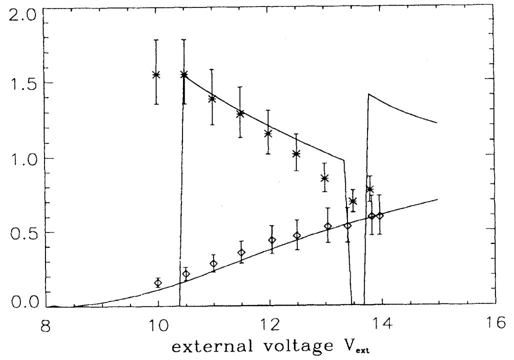

FIG. 26. Comparison between the dominant wave numbers found in experimental patterns and theoretical estimates (solid lines). The upper (lower) curve corresponds to the defocusing (focusing) case. The external voltage is in volts.

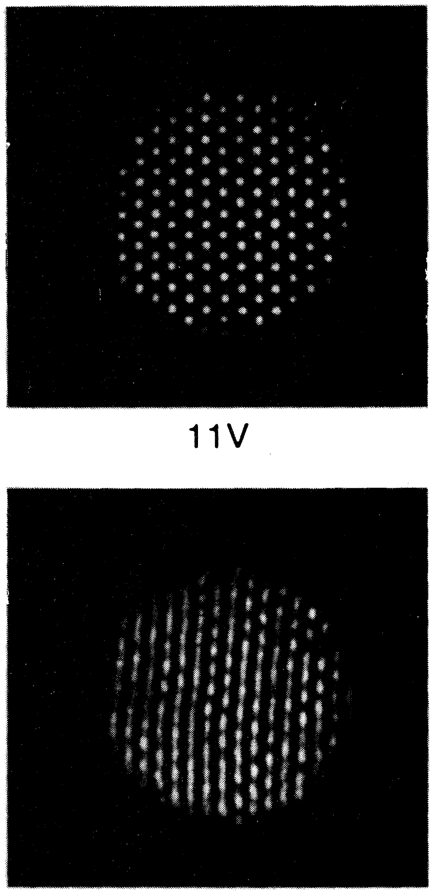

FIG. 27. Experimental hexagon-roll transition due to saturation in the pure phase modulation and defocusing case. Hexagons are obtained for $V_{\rm ext} = 11$ V and rolls for $V_{\rm ext} = 12$ V. The visible beam diameter is 8 mm.

are only two free parameters, i.e., κ_d and V_{th}, which relate the bias intensity J_b to the external voltage [see Eq. (13)]. Note that transverse wave numbers have not been fitted on the experimental data and that the unstable wave numbers found experimentally are all lying within the theoretically predicted range. For the focusing case, we considered values of $\kappa_d/V_0 = 0.08$ and $V_{\mathrm{th}}/\kappa_d = 8.0$ while for the self-defocusing case $\kappa_d/V_0 = 0.22$ and $V_{\mathrm{th}}/\kappa_d = 9.5$. Independent measurements provided values of $\kappa_d/V_0 = 0.222$ and $V_{\mathrm{th}}/\kappa_d = 7.8$. Except for the value of κ_d in the self-defocusing case, quite a good agreement is found with the actual fit of the parameters. It is, however, still unknown how much these parameters depend on the temperature and the frequency of the external voltage. In spite of this, experimental results show an overall tendency in good agreement with our predictions.

Finally, we present experimental evidence of pattern transitions due to saturation in Fig. 27. As already stressed in the previous sections, our model in the Kerr approximation and for pure phase modulation reduces to the equations studied by D'Alessandro and Firth [19,20] which predicts hexagon formation only. By setting the polarization angles in the experiment to zero and by working close to saturation hexagons lose stability to rolls for high values of the external voltage for defocusing nonlinearities. This transition can only be explained by the inclusion of saturation effects in LCLV as described in the previous sections.

VIII. CONCLUSIONS

Diffractive feedback coupled with polarization modulation in LCLV leads to a large variety of spontaneous pattern formation. By including saturation and internal threshold in the description of the LCLV, we have derived a model capable of describing the appearance of rolls, squares, hexagons, tiled patterns, and their competition. In a comparison with models derived in the Kerr approximation, major differences have been found in terms of thresholds and type of patterns. Unexpected instabilities below the LCLV internal threshold have also been described. The agreement with experimental results on a broad area LCLV is good and allows for a high degree of flexibility as well as control of the process of optical pattern formation. In particular, we draw attention to the possibility of choosing pattern type and scale by simple reorientation of the polarizer and change of the external voltage of the LCLV. Many transitions among patterns have been observed in the simulations and in the experiment. Disordered states due to the competing patterns are presently undergoing characterization by exploiting their proximity to well-established geometries.

Control over the process of pattern formation paves the way to applications of spatiotemporal effects in nonlinear optics. Two main topics are of special interest. The first regards the possibility of addressing localized spots of light (see Fig. 21). Isolated spots appear to be only weakly interacting, offering the possibility of local storage of information in the LCLV system. Establishing the relation (if any) with analogous phenomena [42,41] is presently under investigation. The advantage of using our model is its clear connection with experimental realizations. The second subject of experimental and also theoretical interest is the generation and characterization of weakly turbulent states. Transitions to disordered states are observed in the simulations not only when patterns compete but also by breaking of regularly arranged peaks of light, before saturation sets in. We are studying the effect of injection of light modulated at the original (and now unstable) spatial wave vector in order to induce stabilization and consequently control of disordered states.

ACKNOWLEDGMENTS

We have benefited from discussions with W.J. Firth, G. D'Alessandro, A.J. Scroggie, E. Yao, M.A. Vorontsov, G.K. Harkness, and A. Schreiber. This work has been partially supported by the EEC/ESPRIT project TONICS, EPSRC (Grant No. J/30998), Royal Society, and the Deutsche Forschungsgemeinschaft under the program "SFB 185 Nichtlineare Dynamik."

---

[1] J. Opt. Soc. Am. B **7**, 951 (1990), special issue on transverse effects in nonlinear-optical systems, edited by N.B. Abraham and W.J. Firth.

[2] *Transverse Patterns in Nonlinear Optics*, edited by N.N. Rosanov, A.A. Mak, and A.Z. Graznik, SPIE Proc. Vol. 1840 (SPIE, Bellingham, WA, 1993).

[3] *Nonlinear Dynamics and Spatial Complexity in Optical Systems*, Proceedings of the 41 Scottish Summer School in Physics, edited by R.G. Harrison and J.S. Uppal (SUSSP-IOP Publications, Edinburgh, 1993).

[4] Chaos Solitons Fractals **4**, 1249 (1994), special issue on nonlinear optical structures, patterns, chaos, edited by L.A. Lugiato.

[5] *Self-organization in Optical Systems and Applications in Information Technology*, edited by M.A. Vorontsov and W.B. Miller (Springer, New York, in press).

[6] L.A. Lugiato, in *Quantum Optics*, Proceedings of the XXth Solvay Conference on Physics, edited by P. Mandel [Phys. Rep. **219**, 293 (1992)].

[7] S.A. Akhmanov, M.A. Vorontsov, and V.Yu. Ivanov, Pis'ma Zh. Eksp. Teor. Fiz. **47**, 611 (1988) [JETP Lett. **47**, 707 (1988)].

[8] M.A. Vorontsov, N.I. Zheleznykh, and V.Yu. Ivanov, Opt. Quantum Electron. **22**, 501 (1990).

[9] S.A. Akhmanov, M.A. Vorontsov, V.Yu. Ivanov, A.V. Larichev, and N.I. Zheleznykh, J. Opt. Soc. Am. B **9**, 78 (1992).

[10] M.A. Vorontsov and W.B. Miller, in *Self-organization in Optical Systems and Applications in Information Technology* (Ref. [5]), pp. 1–26.

[11] G. Haeusler and A. Vasiliev, University of Erlangen-Nuernberg, Angewandte Optik Annual Report 1989 (un-

published).
[12] B. Thuering, R. Neubecker, and T. Tschudi, Opt. Commun. **102**, 111 (1993).
[13] E. Pampaloni, S. Residori, and F.T. Arecchi, Europhys. Lett. **24**, 647 (1993).
[14] F.T. Arecchi, A.V. Larichev, and M.A. Vorontsov, Opt. Commun. **105**, 297 (1994).
[15] E. Pampaloni, P.-L. Ramazza, S. Residori, and F.T. Arecchi, Europhys. Lett. **25**, 587 (1994).
[16] R. Neubecker, B. Thuering, and T. Tschudi, Chaos Solitons Fractals **4**, 1307 (1994).
[17] G. D'Alessandro, E. Pampaloni, P.-L. Ramazza, S. Residori, and F.T. Arecchi (unpublished).
[18] W.J. Firth, J. Mod. Opt. **37**, 151 (1990).
[19] G. D'Alessandro and W.J. Firth, Phys. Rev. Lett. **66**, 2597 (1991).
[20] G. D'Alessandro and W.J. Firth, Phys. Rev. A **46**, 537 (1992).
[21] F. Papoff, G. D'Alessandro, G.-L. Oppo, and W.J. Firth, Phys. Rev. A **48**, 634 (1993).
[22] M.A. Vorontsov and W.J. Firth, Phys. Rev. A **49**, 2891 (1994).
[23] I.-C. Khoo and S.-T. Wu, *Optics and Nonlinear Optics of Liquid Crystals* (World Scientific, Singapore, 1993).
[24] *Liquid Crystals Application and Uses,* edited by B. Bahadur (World Scientific, Singapore, 1990.)
[25] W.P. Bleha, Laser Focus **19** (10), 111 (1983), and references therein.
[26] Appl. Opt. **31**, 3879 (1992), special issue on spatial light modulators, edited by S. Esener, J.L. Horner, and K.M. Johnson.
[27] M. Tamburrini, M. Bonavita, S. Wabnitz, and E. Santamato, Opt. Lett. **18**, 855 (1993).
[28] E. Ciaramella, M. Tamburrini, and E. Santamato, Appl. Phys. Lett. **63**, 1604 (1993).
[29] A. Gerrard and J.M. Burch, *Introduction to Matrix Methods in Optics* (John Wiley & Sons, London, 1975).
[30] Yu. Dumarevskii, N.F. Kovtonyuk, I.N. Kompanets, A.V. Parfenov, and G.A. Petrovicheva, Kvant. Elektron. (Moscow) **11**, 730 (1984) [Sov. J. Quantum Electron. **14**, 493 (1984)].
[31] P.G. de Gennes, *The Physics of Liquid Crystals* (Clarendon Press, Oxford, 1974).
[32] L.M. Blinov, *Electro-optical and Magneto-optical properties of Liquid Crystals* (Oxford University Press, New York, 1974.)
[33] K. Lu and B.E.A. Saleh, Appl. Opt. **30**, 2354 (1991).
[34] M. Born and E. Wolf, *Principles of Optics* (Pergamon Press, Oxford, 1970).
[35] W.J. Firth, I. Galbraith, and E.M. Wright, J. Opt. Soc. Am. B 2, 1005 (1985).
[36] D. Weaire and M. Al-Hourani, J. Opt. Soc. Am. B **7**, 1066 (1990).
[37] Yu.I. Balkarei, M.G. Evtikhov, J.V. Moloney, and Yu.A. Rzhanov, J. Opt. Soc. Am. B **7**, 1298 (1990).
[38] T.H. Barnes, T. Eiju, S. Kokaji, N. Matsuda, and N. Yoshida, Optik (Stuttgart) **96**, 107 (1994).
[39] H. Mada, Y. Nakajima, and T. Ozawa, Jpn. J. Appl. Phys. **26**, L139 (1987).
[40] H.M. Gibbs, *Optical Bistability: Controlling Light with Light* (Academic Press, Orlando, 1985).
[41] M. Tlidi, P. Mandel, and R. Lefever, Phys. Rev. Lett. **73**, 640 (1994).
[42] N.N. Rosanov and G.V. Khodova, J. Opt. Soc. Am. B **7**, 1057 (1990).
[43] A.J. Scroggie, W.J. Firth, G.S. McDonald, M. Tlidi, R. Levefer, and L.A. Lugiato, Chaos Solitons Fractals **4**, 1323 (1994).
[44] A.R. Gourlay, J. Inst. Math. Appl. **6**, 375 (1970).

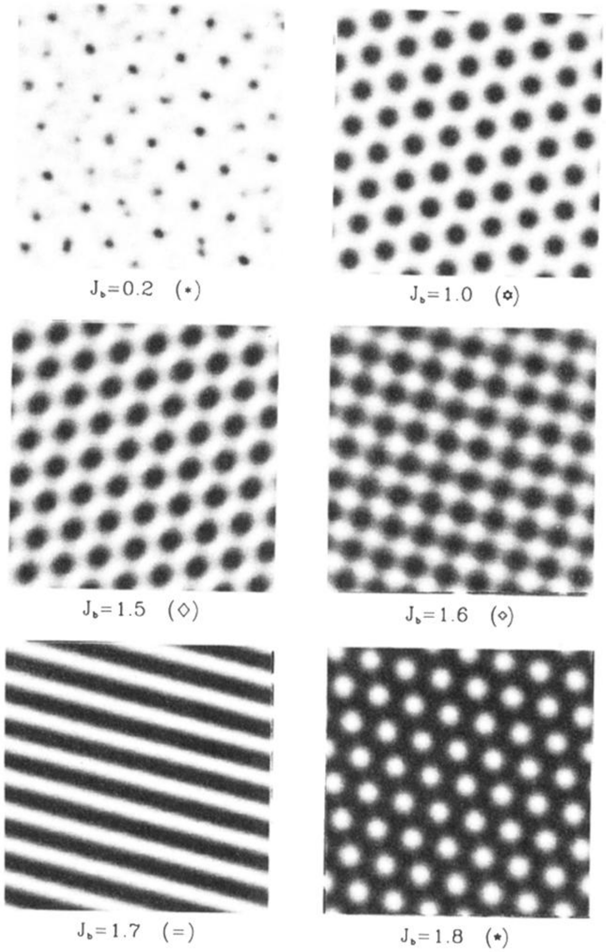

$J_b = 0.2$ (•)

$J_b = 1.0$ (✡)

$J_b = 1.5$ (◇)

$J_b = 1.6$ (⋄)

$J_b = 1.7$ (=)

$J_b = 1.8$ (⋆)

FIG. 14. Different types of patterns found for pure phase modulation $\psi_1 = \psi_2 = 0$ with a defocusing nonlinearity under the variation of J_b. Each square has sides of length 4.8 in normalized space units.

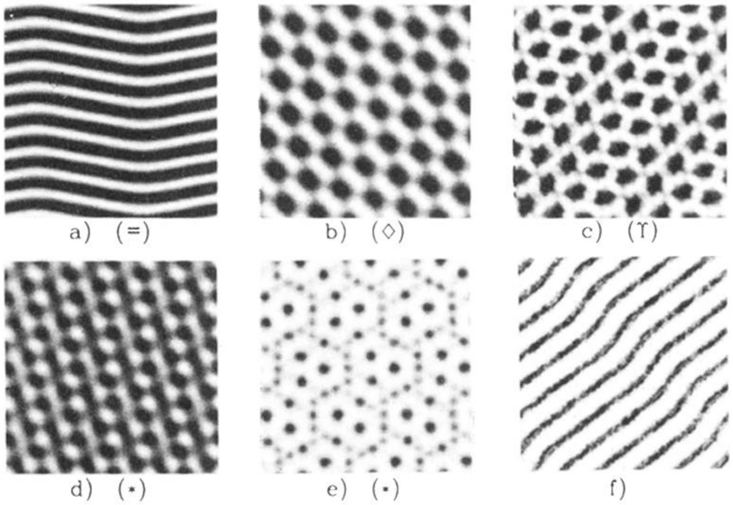

a) (=)
b) (◇)
c) (Υ)
d) (∗)
e) (•)
f)

FIG. 15. Samples of typical patterns obtained just above threshold: (a) rolls showing zigzag instability ("wavy" rolls) for $\psi_1 = -\psi_2 = 40°$, focusing case, $J_b = 1.5$, (b) rhombic structure for $\psi_1 = -\psi_2 = 45°$, defocusing case, $J_b = 1.5$, (c) partially ordered ragged spots for $\psi_1 = -\psi_2 = 45°$, defocusing case, $J_b = 1.05$, (d) complex ordered structure for $\psi_1 = -\psi_2 = 22.5°$, defocusing case, $J_b = 0.7$, 2.5% above threshold, (e) complex ordered structure for same parameters as (d), but 10% above threshold. (f) Roll pattern for negative bias intensity $J_b = -5$, $\psi_1 = -\psi_2 = 45°$, defocusing case. Each square has sides of length 4.8 in normalized space units.

up, $\mu_0 I_{in} = 0.625$ up, $\mu_0 I_{in} = 3.0$ down, $\mu_0 I_{in} = 0.625$

FIG. 18. Examples of patterns developing while overrunning the unstable regime for increasing (up) and decreasing (down) pump, intensity as indicated. Each square has sides of length 9.6 in normalized space units.

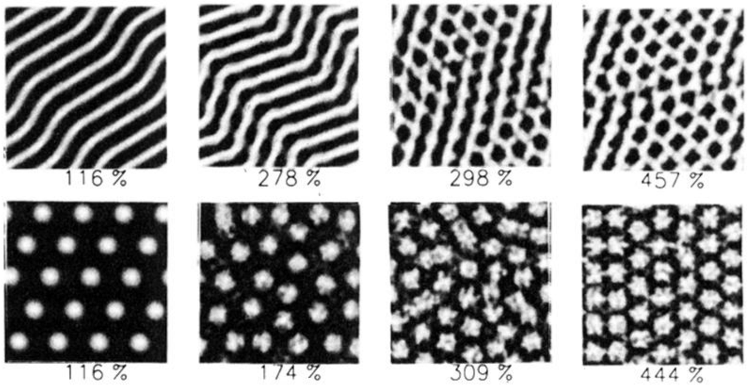

FIG. 20. Samples of patterns obtained for input intensities far above threshold, focusing nonlinearity, $\psi_1 = -\psi_2 = 45^\circ$, $J_b = 1.6$ (upper) and $J_b = 1.1$ (lower). Percentages of the pump intensities relative to the corresponding threshold values are also indicated. Each square has sides of length 6.4 in normalized space units.

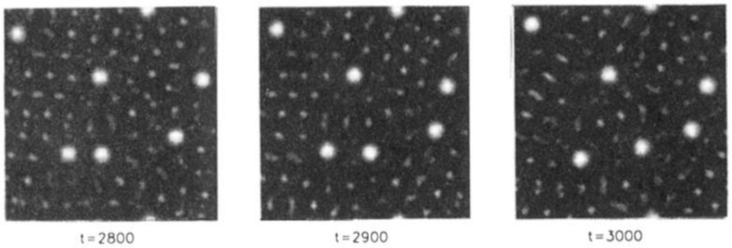

FIG. 21. Temporal sequence of wandering isolated states for focusing nonlinearity, $\psi_1 = -\psi_2 = 40°$, $J_b = 1.0$, and just above threshold. Time is shown in units of τ. Each square has sides of length 8.8 in normalized space units.

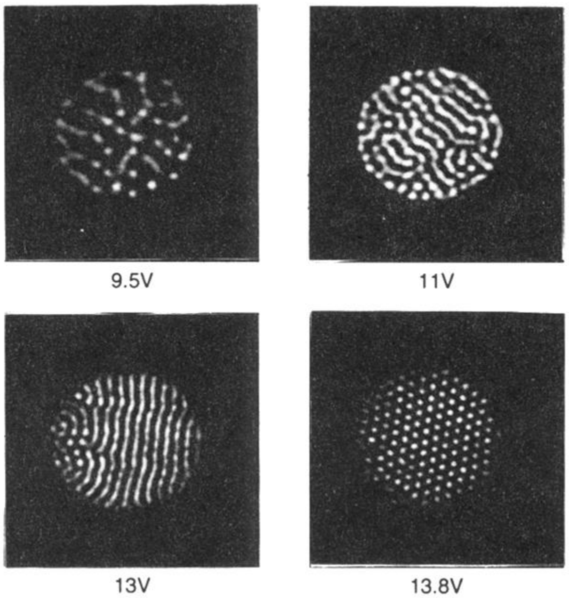

9.5V 11V

13V 13.8V

FIG. 23. Examples of experimentally found patterns for the focusing case and values of the external voltage V_{ext} as indicated. The visible beam diameter is 6 mm.

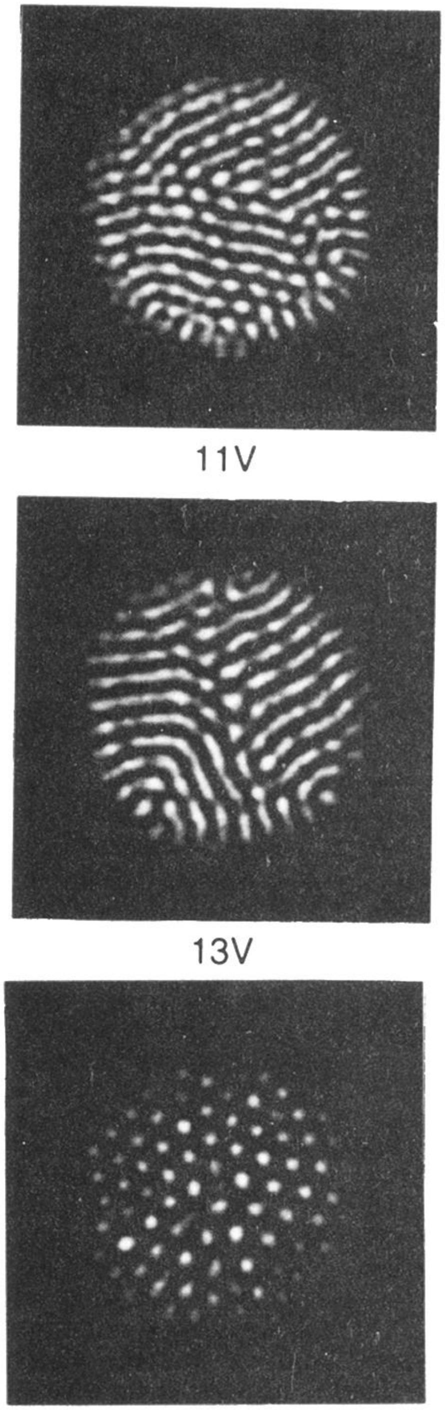

FIG. 24. Examples of experimentally found patterns for the defocusing case and values of the external voltage V_{ext} as indicated. The visible beam diameter is 8 mm.

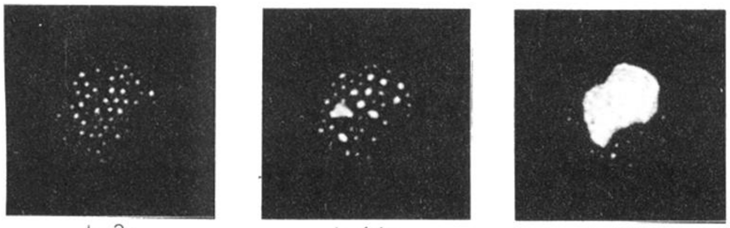

t=2s t=14s t=60s

FIG. 25. Transient evolution towards a homogeneous state of an experimental hexagonal pattern (defocusing case, $V_{\text{ext}} = 13.92$ V). The visible beam diameter is 6 mm.

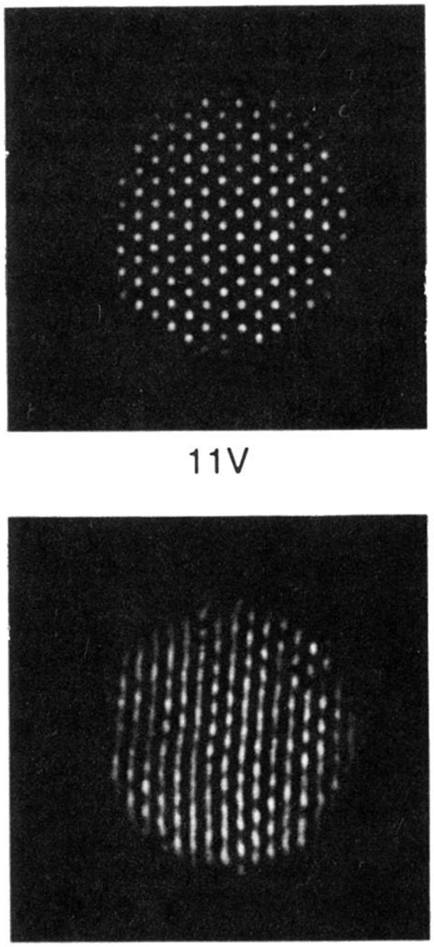

FIG. 27. Experimental hexagon-roll transition due to saturation in the pure phase modulation and defocusing case. Hexagons are obtained for $V_{\mathrm{ext}} = 11$ V and rolls for $V_{\mathrm{ext}} = 12$ V. The visible beam diameter is 8 mm.